

POINT PROCESS MODELS FOR SPATIO-TEMPORAL DISTANCE SAMPLING DATA

BY YUAN YUAN[†], FABIAN E. BACHL[‡], FINN LINDGREN[‡], DAVID L. BORCHERS[†], JANINE B. ILLIAN^{†,§}, STEPHEN T. BUCKLAND[†], HÅVARD RUE[§], AND TIM GERRODETTE[¶]

University of St Andrews[†], University of Edinburgh[‡], Norwegian University of Science and Technology[§] and Southwest Fisheries Science Center, NOAA National Marine Fisheries Service[¶]

Distance sampling is a widely used method for estimating wildlife population abundance. Design-based distance sampling methods allow abundance to be estimated within any unit that has adequate replication for reliable estimation, which constrains the spatial resolution at which animal density can be estimated, but there is often interest in the underlying spatial structure of populations at finer spatial resolution than this. More sophisticated model-based approaches are required to draw inferences in this case. We formulate the process generating distance sampling data as a thinned spatial point process and propose model-based inference based on a spatial log-Gaussian Cox process. Our method uses a flexible stochastic partial differential equation (SPDE) approach to account for the spatial autocorrelation, and integrated nested Laplace approximation (INLA) for Bayesian inference. We illustrate the method using distance sampling data from a series of shipboard line transect surveys in the eastern tropical Pacific (ETP).

1. Introduction. Distance sampling is a widely-used set of survey methods for estimating animal density or abundance (Buckland et al., 2001, 2015b). Conventional distance sampling methods (of which line transect and point transect methods are the most common) use a combination of model-based inference for estimating detection probability and design-based inference with Horvitz-Thompson-like estimators (Borchers et al., 1998) for estimating density and abundance conditional on the detection probability estimates. While the design-based nature of the second stage in this two-stage estimation process (see Buckland et al., 2016) confers robustness on density and abundance estimates when suitable designs are used, it severely restricts the spatial resolution at which such estimates can be obtained. This is because design-based inference requires adequate sampling units (strips for line transect surveys and circular plots for point transect surveys) in each area for which animal density or abundance is to be estimated. The low spatial resolution of estimates from this two-stage approach limits the utility of estimates obtained from conventional distance sampling methods as there is often interest in the distribution at high spatial resolution. As a result, there has been increasing interest in distance sampling methods that generate continuous spatial density surface estimates, and hence allow inference at an arbitrarily fine spatial scale.

In this paper, we consider a series of line transect surveys of blue whales (*Balaenoptera musculus*) in the Eastern Tropical Pacific Ocean (ETP, Gerrodette and Forcada, 2005), in which the focus of inference is in how density changes continuously in space, with respect to available explanatory variables, and across years. Estimating blue whale abundance and distribution from these data is challenging because the surveys were designed for dolphins affected by the tuna purse-seine fishery; the strata and survey effort were not optimized for blue whales. A continuous spatial model has the potential to borrow strength from data outside the lightly-sampled strata to improve overall inference.

One can obtain a continuous density model by extending the two-stage approach (estimating detection probability in the first stage and density or abundance in the second) to base the second stage on a spatial model of density rather than on the design. This is usually done by discretizing the sampled strips into smaller

*The project is funded by the Engineering and Physical Sciences Research Council (EPSRC) –EP/K041061/1 and EP/K041053/1.

Keywords and phrases: distance sampling, spatio-temporal modeling, stochastic partial differential equations, INLA, spatial point process

spatial units in the case of line transects and specifying a model for the counts within each unit, with estimated detection probability as an offset to correct the counts for detectability. [Hedley et al. \(2004\)](#) and [Hedley and Buckland \(2004\)](#) pioneered this approach and [Niemi and Fernández \(2010\)](#) developed a similar approach (but ignoring detection uncertainty). The R-package `dsm` ([Miller et al., 2014](#)) implements the approach of [Hedley et al. \(2004\)](#) and [Hedley and Buckland \(2004\)](#) using generalized additive models (GAM, [Wood, 2006](#)) to estimate a density surface using count data from discretized transects. Either frequentist or Bayesian approaches can be used for the second stage ([Oedekoven et al., 2013, 2015](#)), and bootstrapping is often used to propagate the uncertainty of detectability estimated from the first stage. Rather than bootstrapping, [Williams et al. \(2011\)](#) use a more direct approach to incorporate uncertainty of detectability: a random effect term is added in the second stage to characterize the uncertainty in the estimation of the detection function from the first stage.

One can also estimate the parameters of the detection function and the count model simultaneously ([Conn et al., 2012](#); [Johnson et al., 2010](#); [Moore and Barlow, 2011](#); [Oedekoven et al., 2014](#); [Pardo et al., 2015](#); [Royle et al., 2004](#); [Royle and Dorazio, 2008](#); [Schmidt et al., 2012](#)). This is known as a full-likelihood approach, as it involves specifying a likelihood that incorporates both a detection function model and a spatial density model, allowing simultaneous estimation of both models.

Whether inference is in two stages or one, models that discretize searched strips or lines involve an element of subjectivity in choosing the size of the discrete units and a loss of spatial information because each discrete unit can have only one value of any spatial covariate attached to it, even though it might span an area incorporating a range of covariate values. In this paper we develop a method that does not suffer from these problems, using a point process model.

Point process theory provides a flexible modeling framework for incorporating the underlying spatial or spatio-temporal stochastic processes that does not require discretization of spatial sampling units. Point process models have been used with ecological data to estimate smooth spatial density surfaces and are an obvious choice for the spatial model component of a full likelihood line transect model, although to date they have mainly been used in ecological applications with fully mapped point patterns ([Wiegand and Moloney, 2014](#)), which one does not get from line transect surveys. Such models have been used with a two-stage approach: [Stoyan \(1982\)](#) formulated line transect data as observations of stationary point processes; [Hedley et al. \(2004\)](#) considered point process models for point transect surveys, and [Högmader \(1991, 1995\)](#) constructed a marked point process model for line transect data with detection probability of an animal treated as a mark, but they used a detection model (in which each animal has a detection circle with variable radius) that was shown by [Hayes and Buckland \(1983\)](#) to be unrealistic and often resulting in biased inference.

Here we develop a full likelihood point process model for line transect data, in which the detection process thins the underlying point process, and in which the detection model and the point process model are estimated simultaneously. Such an approach is not new for modeling distance sampling data. The R-package `DSpat` ([Johnson et al., 2010, 2014](#)) uses a thinned point process model for line transect survey data. However, their method assumes spatial independence among observations conditional on point process intensity, which is usually not the case in practice, and may result in biased estimates. We relax the independence assumption by using the stochastic partial differential equation approach (SPDE, [Lindgren et al., 2011](#)) to incorporate a spatial or spatio-temporal random field for the underlying stochastic process of autocorrelated spatial or spatio-temporal random effects. For point process data in general, the SPDE approach avoids the need to aggregate observations ([Simpson et al., 2016](#)), and it provides a flexible modeling framework for spatio-temporal random fields. We build our models in a Bayesian framework, which gives us a tool for fitting complicated models, and the advantage of being able to use integrated nested Laplace approximation (INLA, [Rue et al., 2009](#)) for inference. INLA is a computationally efficient method for Bayesian inference using numerical approximations instead of a sampling-based method such as Markov chain Monte Carlo algorithms. In addition, our modeling framework accommodates the models of the sort used by [Johnson et al. \(2010\)](#), as well as the second stage of the two-stage approach of [Miller et al. \(2013\)](#).

In Section 2, we build a spatio-temporal point process model for distance sampling data, and the likelihood is evaluated using the computational methods described in Section 3. Then in Section 4, we analyze the ETP blue whale data, allowing a better understanding of the underlying spatial stochastic process of blue whale density in the ETP survey area, and how the blue whales respond to sea surface temperature in space and time. Finally, in Section 5, we discuss our modeling approach for spatially-referenced distance sampling data and extensions for more complicated cases.

2. Models. Spatial point processes model the locations of objects in space (Diggle, 2003; Illian et al., 2008; Møller and Waagepetersen, 2004; Stoyan and Grabarnik, 1991; van Lieshout, 2000). Before describing the effect of distance sampling, we consider spatial point patterns formed by objects, represented as collections of locations, $\mathbf{Y} = \{s_i, i = 1, \dots, n\}$. The point set \mathbf{Y} is considered as a realisation from a random point process on a bounded domain Ω , where usually $\Omega \subset \mathbb{R}^2$. Since the ETP survey domain is large enough for the curvature of the Earth to matter (see Figure 1), we will treat Ω as a subdomain of a sphere, $\Omega \subset \mathbb{S}^2$.

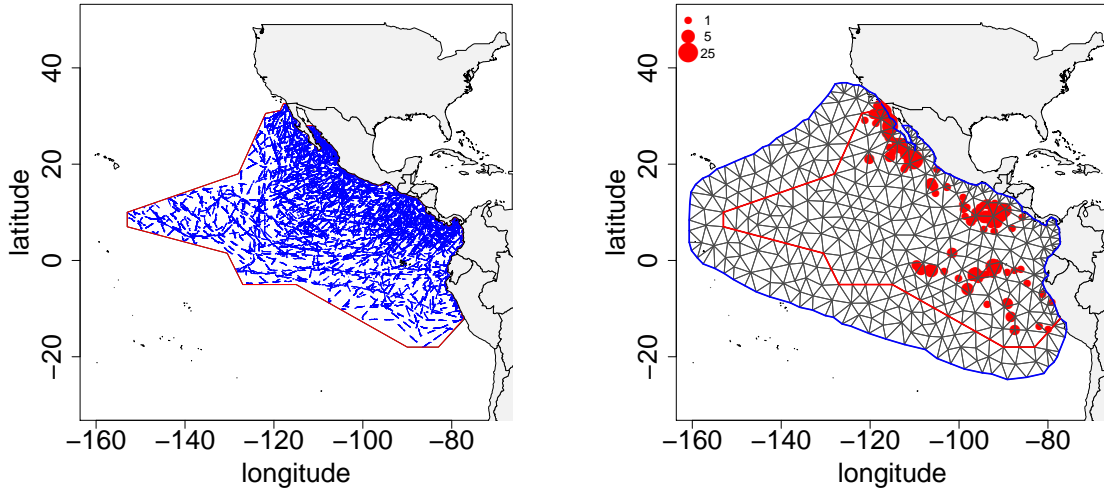


FIG 1. Plot of the ETP data: the left panel plots the transect segments from the effort data where the blue lines specify the transect lines surveyed from 1986 to 2007, and the right panel displays the blue whales sighting data on top of the mesh used in our analysis where the red dots represent the detected groups: the radius of each dot is proportional to the logarithm of the group size plus 1. There was a total of 182 sightings of blue whale groups over all years, with a mean group size of 1.8 and sd 2.1. The red line in both panels gives the boundary of the ETP survey region.

2.1. Spatial hierarchical Poisson point process models. For any subset $A \subseteq \Omega$, the number of objects in A is denoted $N_{\mathbf{Y}}(A)$. For an inhomogeneous point process, we define an intensity function $\Lambda(\mathbf{s})$ as

$$\Lambda(\mathbf{s}) = \lim_{\epsilon \rightarrow 0} \frac{E\{N_{\mathbf{Y}}[\mathcal{B}_{\epsilon}(\mathbf{s}, t)]\}}{|\mathcal{B}_{\epsilon}(\mathbf{s}, t)|}, \quad \mathbf{s} \in \Omega,$$

where $\mathcal{B}_{\epsilon}(\mathbf{s})$ is a ball of radius ϵ centered at \mathbf{s} . For all non-overlapping subsets $A_1, \dots, A_m \subset \Omega$, an inhomogeneous Poisson point process has the following two conditions,

$$N_{\mathbf{Y}}(A_k) \sim \text{Po} \left[\int_{A_k} \Lambda(\mathbf{s}) d\mathbf{s} \right], \quad k = 1, \dots, m, \text{ and}$$

$$N_{\mathbf{Y}}(A_1), \dots, N_{\mathbf{Y}}(A_m) \text{ are mutually independent.}$$

Finally, we let $\Lambda(s)$ be a random process, and define the point pattern model conditionally on $\Lambda(s)$. The conditional likelihood for the entire point pattern \mathbf{Y} is given by

$$(2.1) \quad \pi(\mathbf{Y}|\Lambda) = \exp\left(|\Omega| - \int_{\Omega} \Lambda(s) ds\right) \prod_{i=1}^{N_{\mathbf{Y}}(\Omega)} \Lambda(s_i),$$

where s_i is the location of the i th observation. If $\log \Lambda(s)$ is modeled with a latent Gaussian linear model, the resulting hierarchical model is a doubly-stochastic log-Gaussian Cox process (Møller and Waagepetersen, 2004).

2.2. Point process models in the context of distance sampling. For wildlife surveys, only a proportion of the population in the domain of interest is observed, due to partial sampling of the domain, and failure to detect all animals in the sampled regions. Distance sampling provides a method to account for imperfect detection. In line transect surveys, an observer traces a path through space, searching a strip centered on the path. The probability of detecting an object typically decreases with distance from the observer. From a modeling perspective, this results in a *thinned* spatial point process with the intensity function scaled by the detection probability.

When deriving the appropriate likelihood model for an observed point pattern, the problem-specific underlying generative structure influences the potential dependence between point locations both over space and in time. It is therefore important to note that the thinning in transect surveys is neither a thinning of a fixed spatial point pattern, nor a thinning of a regular spatio-temporal point process. Instead, each object is characterised by a temporally evolving curve in space, describing its movement, and the observations are thinned snapshots of time-slices of the resulting point process of curves. In addition, the intensity may vary over time, and we write $\lambda(s; t)$ for the spatial point intensity for the full time-slice point pattern at time t , and $\Lambda(s; t)$ for the intensity of the observationally thinned version. The assumptions about the movements of the observer and the objects affect what approximations are allowed in practical calculations.

Traditionally, the detection probability for an object located at a given perpendicular distance z from the path of the observer is modeled by a *detection function* $g(z)$. Assuming that the observer is moving with constant speed v along a straight line, standard Poisson process theory yields the probability of detecting an object located at s_0 as a function of the perpendicular distance $z(s_0)$,

$$P(\text{object at } s_0 \text{ detected} \mid s_0 \in \mathbf{Y}) = 1 - \exp\{-h[z(s_0)]/v\} = g(z(s_0), v),$$

where $h(\cdot)$ is an aggregated detection *hazard* along the path, and $g(\cdot, \cdot)$ is the aggregated detection function, with explicit dependence on v . The standard approach is to model either the aggregated detection probability $g(z, v)$, or the aggregated hazard $h(z)$. Under simple assumptions about the observers, Hayes and Buckland (1983) derived the commonly-used *hazard-rate model*, given by $h(z) = -(z/\sigma)^{-b}$, $b, \sigma > 0$. The half-normal detection function $g(z) = \exp[-z^2/(2\sigma^2)]$, $\sigma > 0$ is another widely-used model. While the hazard-rate model is more flexible than the half-normal detection model, only the latter results in a log-linear probability model. For this reason, the hazard-rate model does not fit directly into the existing INLA estimation software (Rue et al., 2009), and instead we will use a semi-parametric detection model, which we introduce in Section 2.6, to give us a more flexible model than the half-normal.

2.3. Line transect point process likelihood. For line transects, assuming that environmental and other observational conditions that might affect detectability remain constant along suitably short and straight *transect segments*, we can formulate a tractably simple version of the likelihood. The region of space swept by the transect path is assumed to consist of a sequence of rectangular transect segment strips $\{\mathcal{C}_1, \dots, \mathcal{C}_K\}$, so that $\mathcal{C}_{k(t)}$ is the transect strip at time t . Writing $\lambda(s; t)$ for the intensity of potentially observable objects, and introducing transect-dependent detection functions $g_{k(t)}(s)$, the intensity for the thinned observational point

process is $\Lambda(\mathbf{s}; t) = \lambda(\mathbf{s}; t)g_{k(t)}(\mathbf{s})$. Under some loose assumptions (see Appendix A), the joint conditional likelihood for the observed point pattern is the product of the conditional likelihoods for each individual transect segment,

$$(2.2) \quad \pi(\mathbf{Y}|\Lambda) = \exp \left(\sum_{k=1}^K |\mathcal{C}_k| - \sum_{k=1}^K \int_{\mathcal{C}_k} \Lambda(\mathbf{s}; t_{\mathcal{C}_k}) d\mathbf{s} \right) \prod_{i=1}^{N_{\mathbf{Y}}} \Lambda(\mathbf{s}_i; t_i),$$

where $N_{\mathbf{Y}} = \sum_{k=1}^K N_{\mathbf{Y}}(\mathcal{C}_k)$ is the total number of observed objects, located at (\mathbf{s}_i, t_i) , $i = 1, \dots, N_{\mathbf{Y}}$. We do not specifically address the issue of *marks* here, i.e. features or quantities associated with detected groups or animals. Marks that do not affect the detection probability can be modeled alongside the object intensity $\lambda(\mathbf{s}; t)$, including possible common fixed effects and dependent random effects (Illian et al., 2012). However, marks that do affect the detection probability, such as the sizes of groups of animals, require a joint likelihood expression for the extended dimension point process of object locations and their marks, which is a topic for further development.

2.4. A Bayesian hierarchical spatio-temporal point process model. Following the classical approach for log-Gaussian Cox processes, we let the logarithm of the intensity $\lambda(\mathbf{s}; t)$ be a Gaussian process, with linear covariates $\mathbf{x}(\mathbf{s}, t)$, and a zero mean additive Gaussian spatial or spatio-temporal random field $\zeta(\mathbf{s}, t)$ (Møller et al., 1998; Møller and Waagepetersen, 2004, 2007). For computational efficiency, we will use the INLA method for numerical Bayesian inference with Gaussian Markov random fields (Illian et al., 2012; Rue et al., 2009; Simpson et al., 2012), but the general methodology is not tied to a specific inferential framework.

In the likelihood given by (2.2), the log of the thinned intensity is given by

$$(2.3) \quad \log[\Lambda(\mathbf{s}; t)] = \log[\lambda(\mathbf{s}; t)] + \log[g_{k(t)}(\mathbf{s})] = \mathbf{x}(\mathbf{s}, t)^T \boldsymbol{\beta} + \zeta(\mathbf{s}, t) + \log[g_{k(t)}(\mathbf{s})],$$

where we assume Gaussian priors for $\boldsymbol{\beta}$, and a Gaussian random field ζ . If the logarithm of the detection probability model is linear in its parameters, this results in a joint linear model with latent Gaussian components.

In general, any link function and spatially coherent linear predictor could be used for Λ . The point process likelihood only requires Λ to be well-defined pointwise, and integrable. In practice, the numerical integration schemes used for practical likelihood evaluation (see Section 3) require piecewise continuity and differentiability. Covariates affecting $\lambda(\mathbf{s}; t)$ need to be available throughout the transect region for parameter inference, and throughout the domain of interest for spatial prediction. For computational reasons, spatial covariates need to be projected onto the same computational function space as the latent field ζ , see Section 3.1. Covariates affecting $g_k(\mathbf{s})$ need to be available for each transect segment. Within-segment variation in detectability would require a more expensive numerical integration scheme in Section 3.1, equivalent to splitting segments until they were sufficiently short for our assumption of constant detectability within each segment to be fulfilled. As noted at the end of Section 2.3, marks for individuals are currently only allowed if they do not affect the detection probability.

The full model is given by the following hierarchy,

$$\pi(\mathbf{Y}, \zeta, \boldsymbol{\beta}, \boldsymbol{\beta}_g, \boldsymbol{\theta}) = \pi(\mathbf{Y} | \zeta, \boldsymbol{\beta}, \boldsymbol{\beta}_g, \boldsymbol{\theta}) \pi(\zeta | \boldsymbol{\theta}) \pi(\boldsymbol{\beta} | \boldsymbol{\theta}) \pi(\boldsymbol{\beta}_g | \boldsymbol{\theta}) \pi(\boldsymbol{\theta}),$$

where $\boldsymbol{\beta}_g$ are parameters controlling the detection model, $\boldsymbol{\theta}$ are further model parameters, such as precision parameters for the latent Gaussian variables. Each of the prior densities $\pi(\zeta | \boldsymbol{\theta})$, $\pi(\boldsymbol{\beta} | \boldsymbol{\theta})$, $\pi(\boldsymbol{\beta}_g | \boldsymbol{\theta})$, and $\pi(\boldsymbol{\theta})$ are controlled by hyperparameters. (Note that in some software packages, including INLA, the parameters $\boldsymbol{\theta}$ themselves are referred to as hyperparameters.)

For given prior distributions, the goal is to compute the posterior densities for the latent variables, optionally with θ integrated out:

$$\pi(\theta | Y) \propto \frac{\pi(Y, \zeta, \beta, \beta_g, \theta)}{\pi(\zeta, \beta, \beta_g | Y, \theta)} \Big|_{(\zeta, \beta, \beta_g) = (\zeta^*, \beta^*, \beta_g^*)},$$

$$\pi(\zeta, \beta, \beta_g | Y) = \int \pi(\zeta, \beta, \beta_g | Y, \theta) \pi(\theta | Y) d\theta,$$

where $(\zeta^*, \beta^*, \beta_g^*)$ is an arbitrary latent variable state vector. In the INLA method (Rue et al., 2009) this is achieved approximately by replacing $\pi(\zeta, \beta, \beta_g | Y, \theta)$ with various Gaussian or near-Gaussian approximations, and integrating numerically over θ .

2.5. Stochastic PDE models. The general model construction requires no particular assumptions on how the spatial or spatio-temporal random field $\zeta(s, t)$ is modeled or treated computationally. The only requirement is that the model can be written as a latent Gaussian random field in such a way that the model likelihood can be evaluated numerically. In the context of INLA, that means that we need to construct a Gaussian Markov random field representation of the continuous space process. The traditional approach is to discretize space into a lattice and count the number of sighted points in each lattice cell, but here we take an alternative approach that allows us to use the true sighting locations, and to let $\lambda(s; t)$ vary continuously through space. The results from Lindgren et al. (2011) show how to take advantage of the connection between Gaussian Markov random fields of graphs and stochastic partial differential equations in continuous space. Some details of such models are given in Appendix B and the computational implications are discussed in Section 3.1.

2.6. Log-linear detection function models. As noted in Section 2.2, the hazard-rate model is not a log-linear model, which means that estimating the parameters does not directly fall under the latent Gaussian model framework of the INLA estimation software (Rue et al., 2009). In contrast, the half-normal detection model is $g_k(s) = \exp[-z_k(s)^2 / (2\sigma_{g,k}^2)]$, where $z_k(s)$ is the perpendicular distance from s to the k th transect line segment, and $\sigma_{g,k}$ are scale parameters. This can be written in log-linear form as $\log[g_k(s)] = \beta_{g,k} z_k^*(s)$, where $z_k^*(s) = -z_k(s)^2 / 2$, and $\beta_{g,k} = 1/\sigma_{g,k}^2$. In order to allow more flexibility within the log-linear framework we introduce a semi-parametric piecewise quadratic model for the logarithm of the detection function, based on a one-dimensional version of the SPDE in the previous section.

For ease of presentation, first assume that the detection probability is the same for all transects k , so that we can write $G[z(s)] = -\log[g_k(s)]$. The prior distribution for $G(z)$ is then defined by the spline-like stochastic differential equation

$$(2.4) \quad \gamma \frac{d^2 G(z)}{dz^2} = \mathcal{W}(t), \quad t \in [0, z_{\max}] \subset \mathbb{R},$$

$$(2.5) \quad G(0) = 0, \quad \left. \frac{dG(z)}{dz} \right|_{z=0} = 0,$$

where z_{\max} is the maximal detection distance, $\gamma > 0$ is a smoothness parameter, and $\mathcal{W}(t)$ is a white noise process. The boundary constraints ensure that the detection probability at distance $z = 0$ is 1, and that the probability is flat near $z = 0$.

Let $(0, z_1, z_2, \dots, z_p)$ be breakpoints for piecewise quadratic B-spline basis functions $B_i(z)$ (Farin, 2002), such that $z_p = z_{\max}$, with the simplest choice of breakpoints being $z_i = iz_{\max}/p$, $i = 0, 1, \dots, p$. The non-parametric model for $G(z)$ can then be used to construct a discrete model

$$(2.6) \quad G(z) = \sum_{i=1}^p \beta_i B_i(z),$$

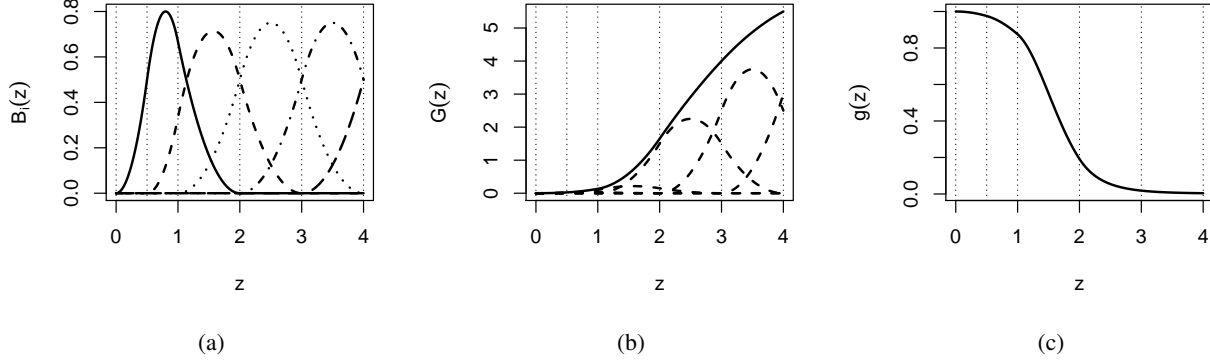


FIG 2. Illustration of the semi-parametric detection function model: (a) B-spline basis functions $B_i(z)$, $i = 1, \dots, 5$, of order 2 that fulfill the boundary conditions (2.5), (b) the weighted functions $\beta_i B_i(z)$ (dashed), their sum $G(z)$ (solid), and (c) the detection probability $g(z) = \exp[-G(z)]$. The breakpoints are $(0, z_1, \dots, z_5) = (0, 0.5, 1, 2, 3, 4)$ and the weights are $(\beta_1, \dots, \beta_5) = (0.05, 0.3, 3, 5, 6)$. Note that the detection function does not automatically have more irregular behavior where the breakpoints are close together, and that this is probabilistically regulated by the stochastic differential equation (2.4).

where the p basis functions only include $B_i(\cdot)$ that fulfil the boundary conditions (2.5), as shown in Figure 2. The joint multivariate Gaussian prior distribution for $(\beta_1, \dots, \beta_p) \sim N(\mathbf{0}, \mathbf{Q}_\beta^{-1}(\gamma))$ is constructed with the same finite element technique that will be used for the spatial SPDE in Section 3.1. For uniform breakpoint spacing, increasing p will make this discrete model converge to the continuous domain model, but for finite p the model is effectively a piecewise quadratic semi-parametric model.

Imposing a monotonicity constraint on $g(z)$ is possible by replacing the basis functions for $G(z)$ with increasing linear combinations of the original basis, and mandating positivity of the β_i coefficients. However, since the latter is currently only implemented in INLA for independent β_i , this is restricted to small p , e.g. 2 or 3, since an independence prior results in a non-smooth function for larger p . An alternative that is feasible when sampling from the posterior distribution is to simply reject all non-increasing samples of $G(z)$. If the data are informative, the smoothing from the prior can in practice be enough to yield monotonic estimates without including an explicit constraint.

Relaxing the assumption that the detection function is the same for all transects is most easily done by adding further linear terms to $\log g_k(s)$ based on observed or constructed covariates that depend on k .

3. Computational methods. There are several practical considerations for evaluating the likelihoods and representing the random fields in such a way that large dense matrices can be avoided. In Section 3.1 we give a brief overview of the essentials for translating stochastic PDEs into manageable Gaussian Markov random fields (GMRF), and Section 3.2 presents a numerical integration scheme for the point process likelihood.

3.1. The stochastic partial differential equation approach. The SPDE/GMRF approach works by replacing the continuous domain stochastic PDE model with a finite dimensional Gaussian Markov random field for basis function weights defined on a triangulation of the domain of interest, such that the sparse precision matrix leads to a good approximation of the continuous space SPDE solutions. Given a triangulation mesh (see the right panel of Fig 1 for the triangulation used for the ETP survey area), Lindgren et al. (2011) define

a finite element representation (Brenner and Scott, 2007) of ζ from (B.1),

$$(3.1) \quad \zeta(\mathbf{s}) = \sum_{j=1}^m w_j \phi_j(\mathbf{s}),$$

where w_1, \dots, w_m are stochastic weights, and ϕ_j , $j = 1, \dots, m$, are deterministic piecewise linear basis functions defined for each node on the mesh: ϕ_j equals 1 at mesh node j and 0 in all the other mesh nodes. The weight vector $\mathbf{w} = (w_1, \dots, w_m)$ is a GMRF with its Markovian properties defined by the mesh structure. It follows that \mathbf{w} determines the stochastic properties of (3.1) and \mathbf{w} is chosen in a way that the distribution of (3.1) approximates the distribution of the solution to the SPDE (B.1). As shown by Lindgren et al. (2011), for the SPDE in (B.1), the resulting weight distribution is $\mathbf{w} \sim N(\mathbf{0}, \mathbf{Q}(\tau, \kappa)^{-1})$, where the sparse precision matrix $\mathbf{Q}(\tau, \kappa)$ is a polynomial in the parameters τ and κ , and is obtained through finite element calculations.

The practical implication of this construction is that instead of directly using the covariances from (B.2), which results in dense covariance matrices and high computational cost, $\mathcal{O}(m^3)$, the SPDE/GMRF approach links the continuous and discrete domains in such a way that the computational cost is reduced to $\mathcal{O}(m^{1.5})$. The computational advantages of GMRFs (Rue and Held, 2005) is strengthened by using INLA for Bayesian inference (Rue et al., 2009). For the case of fully observed log-Gaussian Cox point processes, the in-depth analysis by Simpson et al. (2016) of the combined approximation errors induced by the basis function expansion in combination with the likelihood approximation error shows that the resulting approximate posterior distribution is close to the true posterior distribution. Since the integration scheme in the following section is constructed in the same way, we do not include a detailed approximation error analysis here, but note that the SPDE/GMRF approximation is likely to be the largest source of approximation error. Point patterns are relatively uninformative about the latent intensity, which has the practical effect that the realizations of the fields in the posterior distribution are typically smoother than in directly observed process problems. Hence, the approximation error is very small as long as the triangle mesh edges are short compared with the spatial scales of the covariates and of the point pattern intensity variability.

3.2. Numerical point process likelihood evaluation. Combining the general distance sampling point pattern likelihood (2.2) with the log-linear model structure for $\Lambda(\mathbf{s}; t)$ from (2.3) results in a log-likelihood for the observed point pattern,

$$(3.2) \quad \begin{aligned} \log \pi(\mathbf{Y} \mid \lambda, g) = & \sum_{i=1}^{N_Y} \left\{ \mathbf{x}(\mathbf{s}_i, t_i)^T \boldsymbol{\beta} + \zeta(\mathbf{s}_i, t_i) - \log[g_{k(t_i)}(\mathbf{s}_i)] \right\} \\ & - \sum_{k=1}^K \int_{\mathcal{C}_k} \exp \left\{ \mathbf{x}(\mathbf{u}, t_k)^T \boldsymbol{\beta} + \zeta(\mathbf{u}, t_k) - \log[g_k(\mathbf{u})] \right\} d\mathbf{u} + \sum_{k=1}^K |\mathcal{C}_k|, \end{aligned}$$

where the first term evaluates the log-intensity at the observed locations, and the second term integrates the intensity over the sampled transect segments. The log-likelihood (3.2) is in general analytically intractable as it requires integrals of the exponential of a random field. Therefore, we use numerical integration to evaluate (3.2), and the remainder of this section describes an integration scheme to approximate the integrals efficiently. As noted in Section 2.4, we assume that the covariates $\mathbf{x}(\mathbf{s}, t)$ are expressed using the same piecewise linear basis functions as ζ . For cases where a covariate has a much finer resolution than the one needed for ζ , the efficient integration scheme developed here is not appropriate, and further research is needed to develop an integration method that can deal with that without incurring a high computational cost.

For distance sampling surveys, transect areas describe subsets of the earth's surface. The most natural representation of transect areas would therefore be subsets $\mathcal{C}_k \subseteq \mathbb{S}^2$ of the sphere, leading to surface integration in the Poisson process likelihood. However, the small scale at which earthbound observers are capable of probing their environment lends itself towards easily justifiable simplifications of the numerical integration.

Apart from environmental conditions such as the weather, the curvature of the earth puts an upper bound on the distance at which an observer with a given elevation can actually detect an animal. We therefore approximate the surface integrals over $\mathcal{C}_k \subset \mathbb{S}^2$ by integrals over $\tilde{\mathcal{C}}_k \subset \mathbb{R}^2$, i.e.

$$\begin{aligned} I_{\mathcal{C}_k} &= \int_{\mathcal{C}_k} \lambda(\mathbf{u}; t_k) g_k(\mathbf{u}) d\mathcal{C}_k(\mathbf{u}) = \int_{\tilde{\mathcal{C}}_k} \lambda(\mathbf{u}_k(l, z); t_k) g_k(\mathbf{u}_k(l, z)) \left\| \frac{\partial \mathbf{u}_k}{\partial l} \times \frac{\partial \mathbf{u}_k}{\partial z} \right\| dl dz \\ &\approx \int_{\tilde{\mathcal{C}}_k} \lambda(\mathbf{u}_k(l, z); t_k) g_k(\mathbf{u}_k(l, z)) dl dz, \end{aligned}$$

where we use a transect-specific parameterization \mathbf{u}_k at coordinate l along and distance z to the transect line, respectively. If R is the radius of the earth, then the Jacobian is $\cos(z/R)$, which gives an approximation error of a factor less than $5 \cdot 10^{-6}$ even in the extreme and unrealistic case of an observer at 31 metres above a calm sea looking at the horizon 20 kilometres away.

Another fact that we can utilize is that the detection function g does not depend on the position of the observer along the line but only on the distance of an observation from the line. Similarly, if the transect line is narrow compared to the spatial rate of change in the intensity function, we can substitute the evaluation of λ by an evaluation at the center of the transect line, $\hat{z} = 0$ (see Fig 3). That is,

$$I_{\mathcal{C}_k} \approx \int_{\tilde{\mathcal{C}}_k} \lambda(\mathbf{u}_k(l, \hat{z}); t_k) g_k(\mathbf{u}_k(\hat{l}, z)) dl dz,$$

together with an arbitrary coordinate \hat{l} along the transect line.

REMARK. In a standalone implementation, the integral could be written as a product of two one-dimensional integrals, and even evaluated exactly due to the log-linearity of the model. Unfortunately, the resulting structure cannot be expressed using only evaluations of products of λ and g , which is a requirement imposed by the internal structure of the INLA implementation, so we do not use that approach here.

We can also make use of the fact that λ lives on a mesh. If the mesh triangles are small enough, the log-linear function $\lambda(\cdot)$ is approximately linear within each triangle. By splitting a transect line \mathcal{C}_k into segments $\mathcal{C}_{k,j}$, $j \in 1, \dots, J$, each of which resides in a single triangle (see Fig 3), we obtain a Gaussian quadrature method of order one,

$$I_{\mathcal{C}_k} \approx \sum_{j=1}^J \int_{\tilde{\mathcal{C}}_{k,j}} \lambda(\mathbf{u}_{kj}(l, \hat{z}); t_k) g_k(\mathbf{u}_{kj}(\hat{l}, z)) dl dz \approx \sum_{j=1}^J w_{k,j} \int_z \lambda(\mathbf{u}_{kj}(l_{k,j}, \hat{z}); t_k) g_k(\mathbf{u}_{kj}(\hat{l}, z)) dz.$$

Here, $l_{k,j}$ is half of segment j 's length $w_{k,j}$. The integration over the distance parameter can now be approximated by a quadrature rule with an equidistant scheme, so that

$$I_{\mathcal{C}_k} \approx \sum_{j=1}^J \sum_{r=1}^R \tilde{w}_{k,j} \lambda(\mathbf{u}_{kj}(l_{k,j}, \hat{z}); t_k) g_k(\mathbf{u}_{kj}(\hat{l}, z_r)),$$

where $\tilde{w}_{k,j} = \frac{z_{\max}}{R} w_{k,j}$ with maximal detection distance z_{\max} , and we substitute $\hat{l} = l_{k,j}$. We can then write

$$I_{\mathcal{C}_k} \approx \sum_{j=1}^J \sum_{r=1}^R \tilde{w}_{k,j} \lambda(\tilde{\mathbf{u}}_{k,j,r}; t_k) g_k(\mathbf{u}_{k,j,r}),$$

where $\mathbf{u}_{k,j,r}$ are points on the perpendicular line through the midpoint of transect k 's segment j , and $\tilde{\mathbf{u}}_{k,j,r}$ is the midpoint of each subsegment line.

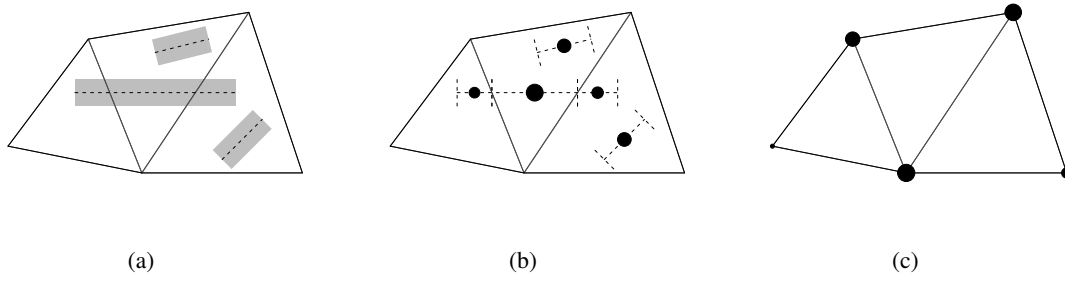


FIG 3. Integration scheme for transect lines. Panel (a) shows three triangles of a mesh together with three transects. When the width of the transects is small compared to the size of the triangles, and thus the slope of the intensity has small variability perpendicular to each segment, the areal integration can be reduced to an integration along the observer's trajectory weighted by the width of the transect. Trajectories that reside in multiple triangles can then be split at the triangle edges such that their midpoints can serve as integration points when assuming linear intensity within the triangles (b). Under the same assumption, integration points from each triangle can be accumulated into re-weighted points at the mesh vertices (c). The areas of the filled circles are proportional to the integration weights.

As a last step we can again make use of the assumption that the function we are integrating over is approximately linear within a given triangle. It is straightforward to show (see Appendix C) that this means that each integration point can be expressed by an evaluation of the function at the triangle vertices weighted by the within-triangle Barycentric coordinates of the original point (Farin, 2002). We can therefore summarize integration points that reside in the same triangle and share a common time coordinate t_k to such evaluations at the mesh vertices, illustrated in Fig 3. This can, depending on the problem structure, lead to a significant reduction in the respective computational workload.

The approximation error from treating the log-linear function within each triangle as linear can be reduced by subdividing each triangle into four. However, evaluating the function at the mid-points of the original triangle edges as well as the original vertices leads to an increase in the computational cost of at least a factor of four, since the number of edges is approximately three times the number of vertices in the mesh.

4. Case study: the blue whale data from the Eastern Tropical Pacific surveys.

4.1. *The ETP surveys.* Line-transect cetacean surveys were carried out in the eastern tropical Pacific Ocean (ETP) between 1986 and 2007 (Fig 1). In 1986-1990, 1998-2000, 2003 and 2006, the entire ETP area of 21.353 million square kilometres was sampled. These complete surveys required two oceanographic research vessels (3 in 1998) for 120 sea days each. Transect search effort was stratified by area (Gerrodette and Forcada, 2005), and in 1992, 1993 and 2007, only part of the ETP area was sampled. The spatial differences in intensity of sampling are accounted for by the spatial model (see Section 3.2 for more detail). Methods of collecting data followed standardized line-transect protocols (Kinzey et al., 2000). Briefly, in workable conditions, a visual search for cetaceans was conducted by a team of three observers on the flying bridge of each vessel during all daylight hours as the ship moved along the transect at a speed of 10 knots. Pedestal-mounted 25X binoculars were fitted with azimuth rings and reticles for angle and distance measurements. If a blue whale sighting was less than 10 km from the transect, the team went off-effort and directed the ship to leave the transect to approach the sighted animal(s). The observers identified the sighting to species or subspecies (if possible) and made group-size estimates. Forney et al. (2012) and Pardo et al. (2015) have also analyzed blue whale sightings from the same ETP surveys. Forney et al. (2012) used GAMs to estimate encounter rate and incorporated group size in the estimation of both detection and density. Pardo et al. (2015) employed separate models of detection and density (Cressie et al., 2009; Royle and Dorazio, 2008), and estimated all parameters simultaneously in a hierarchical Bayesian framework.

Using the modeling framework described in Section 2 and computational methods in Section 3 for evaluating the likelihood, we analyze the blue whale data collected from the ETP survey. The main objective of our analysis is to predict the blue whale group density over years for the ETP survey area, and to study the effect of sea surface temperature (SST) on the blue whale group density. The function of interest for density estimation is the intensity of point process before thinning, i.e., $\lambda(s, t)$ in (2.3), which we refer to as the group density in the ETP blue whale application.

The group size distribution for blue whales has mean 1.8 and standard deviation 2.1. Blue whale groups in the ETP tend to be small, and the size is easily established, so it is realistic to treat the group size of blue whales as known without error (Gerrodette et al., 2002). Given the small group size of the blue whales in the ETP survey, we assume that the group size does not affect the detection probability. The detection of cetaceans on ship surveys also depends on wind conditions, but this is less important for blue whales because of their large body size and conspicuous blow. Therefore, we assume the detection probability only depends on the perpendicular distance for the blue whales in the ETP survey. In our analysis, we truncate the data at perpendicular distance 6 km, i.e. $w = 6$. We also assume that distances were observed without error for each detected animal group and we fit a semi-parametric model given by (2.6) to estimate the detection function.

To build a spatio-temporal model using the SPDE approach described in Section 3.1, we start by constructing a mesh for the ETP survey as shown in Fig 1. The ETP survey is bounded partially by the coastline and partially by the red line of Fig 1. We use a simplified representation of the actual coastline as the mesh boundary to incorporate the boundary effect because a physical boundary such as the coastline has a strong effect – in this case, there will be no blue whales on land! We use a simplified representation of the coastline, because the actual coastline is too ‘angular’ and hence problematic for the SPDE approach (Lindgren and Rue, 2015). Meanwhile, we extend the boundary further in the northwest and south directions in the eastern tropical Pacific, in order to exclude the boundary effect for the part of the survey area that is bounded by the red line in Fig 1. Given the low sighting rate of the blue whales, there is little information contained in the data to fit a complicated spatio-temporal stochastic process for the random field, such as the AR(1) temporal process used by Cameletti et al. (2012); even the simpler version of the spatio-temporal process with replicated spatial field over time is not feasible. We consider a spatial-only Gaussian random field, together with spatial trend covariates (longitude and latitude) and a spatio-temporal covariate, sea surface temperature, with the aim of explaining some of the spatio-temporal dynamics of the blue whale group density in the ETP survey area.

4.2. Incorporating a spatio-temporal environmental covariate: sea surface temperature (SST). Based on the Simple Ocean Data Assimilation (SODA) model (http://apdrc.soest.hawaii.edu/datadoc/soda_2.2.4.php), the SST data are available on a fine grid over the ETP survey area on a monthly scale between 1986 and 2007. First, within each year, SST is averaged over the months July to December, during which the survey was conducted. Second, given the average SST within this period each year over a fine grid on the survey area, we use piecewise linear interpolation to calculate the SST for any given location and year, denoted by $\text{sst}(s, t)$. Fig 4 shows the interpolated $\text{sst}(s, t)$ for each year over the ETP survey area. The figure shows both spatial and the inter-year variation in SST, and we use hierarchical centering to separate the annual and spatial effects of SST. Hierarchical centering is a commonly used technique in multilevel modeling (Kreft et al., 1995), and we consider two different centering schemes here:

1. Within-year centering. This approach results in two SST components, the spatially averaged SST for each year, and the spatial SST patterns centered within each year. Let Ω denote the bounded ETP survey area in Fig 1. We use $\bar{\text{sst}}_c(t)$ to denote the SST averaged over the ETP survey area for year t after centering,

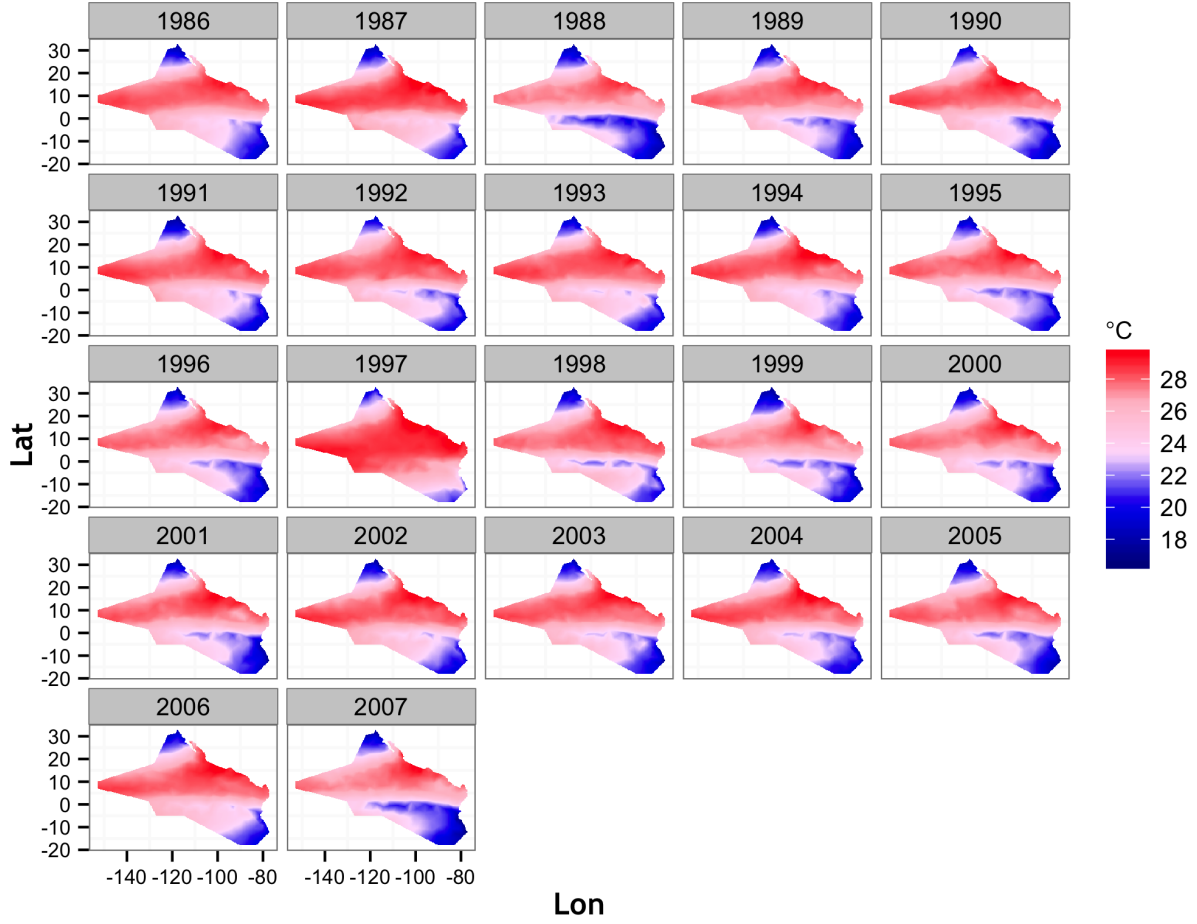


FIG 4. The SST data before centering. For each location and year (1986–2007), the SST is averaged over July to December.

$$(4.1) \quad \overline{\text{sst}}_c(t) = \frac{1}{|\Omega|} \int_{\Omega} \text{sst}(\mathbf{s}, t) \, d\mathbf{s} - \overline{\text{sst}},$$

where $\overline{\text{sst}}$ denotes the overall average of SST, i.e. $\overline{\text{sst}} = \int_{\Omega \times \mathbb{T}} \text{sst}(\mathbf{s}, t) \, d\mathbf{s} \, dt / (|\Omega| \times |\mathbb{T}|)$, with \mathbb{T} denoting the set of survey years. Then the SST centered within year t for location \mathbf{s} , $\text{sst}_{cwy}(\mathbf{s}, t)$, is defined as

$$(4.2) \quad \text{sst}_{cwy}(\mathbf{s}, t) = \text{sst}(\mathbf{s}, t) - \overline{\text{sst}}_c(t).$$

Further information about $\text{sst}_{cwy}(\mathbf{s}, t)$ for each \mathbf{s} and t is plotted in Fig 14 in Appendix D.

2. Space-time centering. This approach results in three SST components by separating the spatial and temporal patterns from a spatio-temporal interaction residual. The three components of SST are the $\overline{\text{sst}}_c(t)$ given by (4.1), the SST averaged over years for each location, $\overline{\text{sst}}_c(\mathbf{s})$ given by (4.3), and the SST residuals, $\text{sst}_{res}(\mathbf{s}, t)$ given by (4.4),

$$(4.3) \quad \overline{\text{sst}}_c(\mathbf{s}) = \frac{1}{|\mathbb{T}|} \int_{\mathbb{T}} \text{sst}(\mathbf{s}, t) \, dt - \overline{\text{sst}},$$

$$(4.4) \quad \text{sst}_{res}(\mathbf{s}, t) = \text{sst}(\mathbf{s}, t) - \overline{\text{sst}}_c(t) - \overline{\text{sst}}_c(\mathbf{s}) + \overline{\text{sst}}.$$

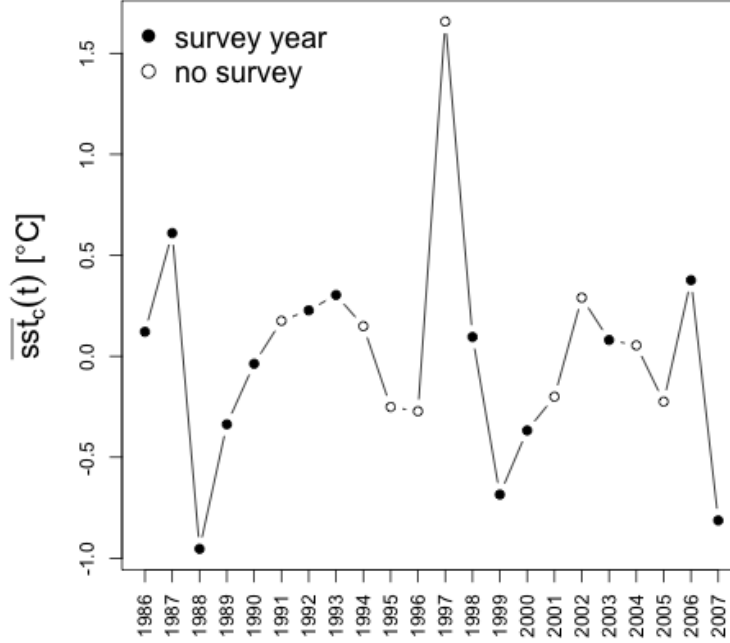


FIG 5. The temporal effect of SST after centering displayed by $\overline{sst}_c(t)$ given by (4.1), the SST averaged over the ETP survey area bounded by the red line in Fig 1, and then centered by the overall average of SST, $\overline{sst} = \int_{\mathbb{T}} \int_{\Omega} sst(s, t) ds dt / (|\mathbb{T}| \times |\Omega|) = 25^\circ\text{C}$. The filled circles represent survey years and the empty circles non-survey years. The plot shows that 1997 is extreme relative to all survey years.

$\overline{sst}_c(t)$ indicates whether a year is relatively warm or cold after averaging over the survey area, and similarly, $\overline{sst}_c(s)$ indicates whether a location is relatively warm or cold after averaging over the survey years. The SST residual, $sst_{res}(s, t)$, contains information about the interaction between temporal pattern and the spatial average of SST. In Appendix D, we plot $\overline{sst}_c(s)$ given by (4.3) in Fig 15, $sst_{res}(s, t)$ given by (4.4) in Fig 16.

As shown in Fig 4, La Niña conditions are characterized by a band of cooler waters in 1988, 1999 and 2007, and El Niño conditions by a much wider band of warm ocean water in 1997 (1987 is a moderately strong El Niño year according to the scale by Wolter and Timlin, 2011). Centering SST strongly captures the El Niño/La Niña oscillations that occur at irregular intervals in the ETP survey area (see Appendix D for more detail). The temporal effect of SST after centering displayed by (4.1) in Fig 5 correctly reflects the La Niña conditions in 1988 and 2007, and strongly highlights the El Niño year 1997 as an outlier. Unfortunately, no survey was conducted in 1997. Given the time series of $\overline{sst}_c(t)$ for the survey years and non-survey years in Fig 5, it is obviously problematic to predict for 1997 using a model fitted on the data from the survey years, which are represented by the filled circles in Fig 5. Therefore, we make predictions for all years except 1997.

4.3. Results. Table 1 lists the results for three different models: Model 0 does not incorporate SST, Model 1 incorporates SST using the within-year centering scheme, and Model 2 uses the space-time centering scheme. All these models have the same SPDE specification of the latent spatial Gaussian random field. Table 1 summarizes the posterior density of the linear regression coefficients, i.e. the β 's.

The effects of longitude and latitude. Model 0 contains only the spatial trend covariates, longitude and latitude. The 95% posterior credible intervals for the regression coefficients from this model both include zero with medians very close to zero. This indicates little evidence for the effect of longitude and latitude on the blue whale group density in the ETP survey area, suggesting no large-scale linear spatial effect that

TABLE 1
The posterior estimates for the fixed-effects coefficients for each model.

Model	Parameter	Mean	Std.dev.	Quantile		
				2.5%	50%	97.5%
Model 0	β_0	-12.28	2.27	-17.96	-11.98	-8.57
	β_{lon}	0.10	0.07	-0.05	0.10	0.26
	β_{lat}	0.01	0.10	-0.22	0.03	0.16
Model 1	β_0	-4.56	3.02	-10.94	-4.44	1.06
	$\beta_{\overline{sst}_c(t)}$	0.79	0.21	0.37	0.79	1.20
	$\beta_{\overline{sst}_{cwy}}$	-0.28	0.10	-0.48	-0.28	-0.07
Model 2	β_0	-11.83	2.22	-17.28	-11.59	-7.89
	$\beta_{\overline{sst}_c(t)}$	0.73	0.21	0.32	0.73	1.16
	$\beta_{\overline{sst}_c(s)}$	-0.60	0.14	-0.88	-0.60	-0.34
	$\beta_{\overline{sst}_{res}}$	0.23	0.17	-0.10	0.22	0.55

can be explained by longitude and latitude. This interpretation is supported by the results from models that include SST. Specifically, when we add longitude and latitude to Models 1 and 2, the 95% posterior credible intervals of the longitude and latitude regression parameters still include zero. We therefore exclude longitude and latitude, and henceforth consider only Models 1 and 2.

Results when using the within-year centering scheme. Model 1 uses the within-year centering scheme described in Section 4.2, and incorporates the effect of SST through $\beta_{\overline{sst}_c(t)}$ and $\beta_{\overline{sst}_{cwy}}$. The posterior estimates of $\beta_{\overline{sst}_c(t)}$ in Model 1 indicate a positive effect of $\overline{sst}_c(t)$ given by (4.1), meaning that more blue whale groups are expected in warmer years. Meanwhile, the results of $\beta_{\overline{sst}_{cwy}}$ indicate a negative effect of $\overline{sst}_{cwy}(s, t)$ defined in (4.2), meaning that more blue whale groups are expected in a colder location within a year.

Results when using the space-time centering scheme. Model 2 uses the space-time centering scheme described in Section 4.2, and incorporates the effect of SST through $\beta_{\overline{sst}_c(t)}$, $\beta_{\overline{sst}_c(s)}$ and $\beta_{\overline{sst}_{res}}$. The results of $\beta_{\overline{sst}_c(t)}$ using space-time centering scheme are similar to those of $\beta_{\overline{sst}_c(t)}$ from the within-year centering scheme. The negative sign of $\beta_{\overline{sst}_c(s)}$ indicates that there are fewer whales in places that have high average temperature across all years than those that have low average temperature. In addition to the spatio-temporal patterns modeled by $\beta_{\overline{sst}_c(t)}$ and $\beta_{\overline{sst}_c(s)}$ in Model 2, the spatio-temporal interaction estimated by $\beta_{\overline{sst}_{res}}$, suggests a positive relationship between $\overline{sst}_{res}(s, t)$ given by (4.4) and blue whale group density.

Summary of the SST effects. The posterior median estimates of $\beta_{\overline{sst}_c(t)}$ are similar with Models 1 and 2, indicating that years that are warmer on average are expected to have more blue whale groups. The negative posterior median of $\beta_{\overline{sst}_c(s)}$ suggests that locations that are colder on average over the years are expected to have more blue whale groups than locations that are warmer on average. From (4.2), (4.3) and (4.4), we have $\overline{sst}_{cwy}(s, t) = \overline{sst}_c(s) + \overline{sst}_{res}(s, t)$, so that $\beta_{\overline{sst}_{cwy}}$ in Model 1 amounts to combining $\beta_{\overline{sst}_c(s)}$ and $\beta_{\overline{sst}_{res}}$ in a single parameter. The results of Models 1 and 2 indicate a negative effect of SST in space for both $\overline{sst}_{cwy}(s, t)$ and $\overline{sst}_c(s)$, and positive effect of space-time interactions. This indicates that both within year and averaging across years, blue whale group density tends to be higher in places with colder water in the ETP survey area.

Posterior median and relative uncertainty of the blue whale group density. The posterior median of blue whale density, $\lambda(s; t)$, for year 1986 is shown in the top panel of Fig 6 for Models 0, 1 and 2, respectively. The top three plots of Fig 7 show little difference in the posterior density surface of the blue whale groups in 1986 derived from the three models. These figures indicate areas of higher blue whale group density in the

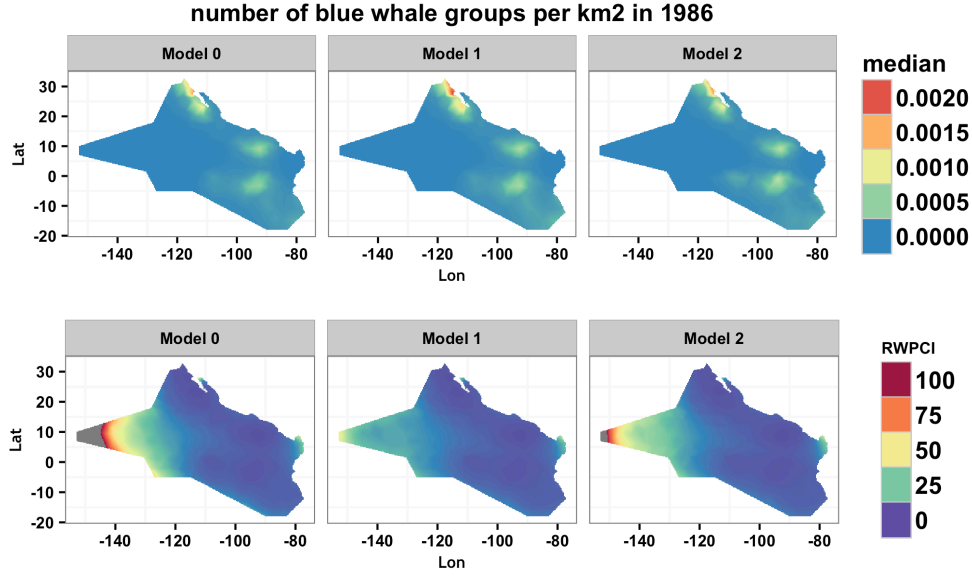


FIG 6. The posterior median (top) and RWPCI from (4.5) (bottom) of the ETP blue whale groups density in 1986 using Models 0, 1, and 2 in Table 1. The RWPCI colour palette is cut off at 100 to exclude the extreme values at the western corner of the ETP survey area.

north off the coast of Baja California, in the area of the Costa Rica Dome off the coast of Central America, and in the south-east in the vicinity of the Galapagos Islands. This pattern of the blue whale group density is consistent across all the models implemented, and reflects what we observe in the sightings data in the right panel of Fig 1. This observed spatial pattern is also in general agreement with previous analysis of blue whale sighting data in the ETP (Forney et al., 2012; Pardo et al., 2015). Similar plots for 1986–2007 (omitting the very strong El Niño year 1997), are displayed in Fig 8, 9 and 10 for Models 0, 1, and 2 in Table 1, respectively. Comparing the left panels of these three figures, we can observe some subtle changes when information about SST is incorporated. For example, we see evidence of higher densities in some years, especially 1987 and 2002, which is absent when we fit Model 0 (the model without SST, see Fig 8).

We use the relative width of the 95% posterior credible interval (RWPCI) as a measure of the relative uncertainty for the predicted $\lambda(s; t)$ of the ETP survey area. We define RWPCI as the inter-quartile range divided by the median,

$$(4.5) \quad \text{RWPCI} = (Q_3 - Q_1)/Q_2.$$

When the posterior distribution is approximately Gaussian, RWPCI is about 1.35 times the ratio of the posterior standard deviation to the posterior median. For years 1986–2007 (excluding 1997), the right panels of Fig 8, 9 and 10 show similar results of RWPCI for these three models. The difference of RWPCI between years is too small to visualise in those figures, which is expected both because the SPDE model is only spatial and because the difference in the posterior median of $\lambda(s; t)$ between years is small. The right panel of Fig 6 gives a clearer display of the spatial structure of RWPCI of the blue whales group density in 1986 using the three models in Table 1, and such pattern persists in years. The far west of the survey region has very high relative uncertainty because it is close to the edge of the mesh boundary shown in Fig 1 and has no sighting at all in that area. This is consistent with the very high standard deviation of the spatial random field in that area shown in Fig 7. As shown in this figure, regions of low $\lambda(s; t)$ tend to have higher uncertainty associated with the latent field, which is expected due to modeling on the log scale (see equation 2.3). The

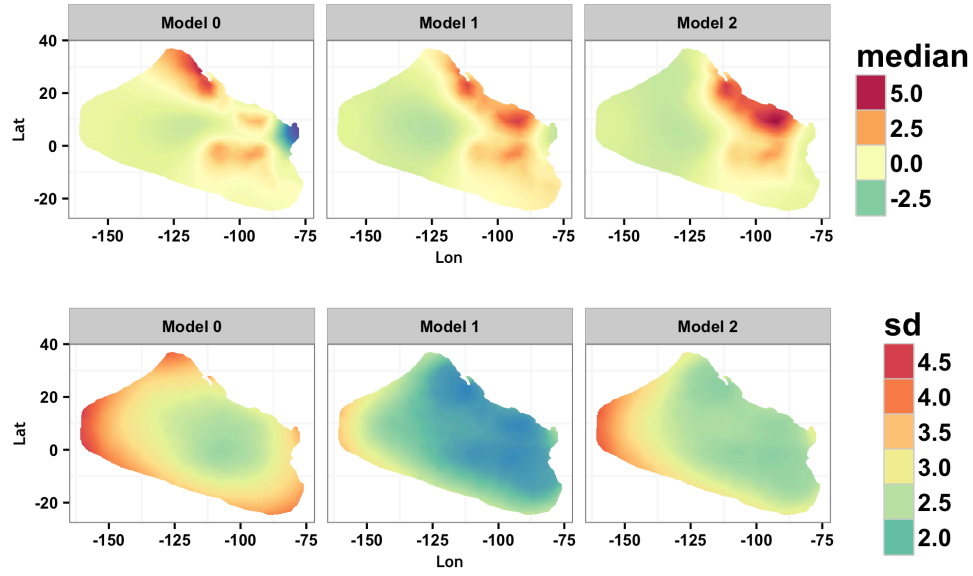


FIG 7. The posterior median and standard deviation of the latent field (3.1) when using Models 0, 1 and 2 in Table 1.

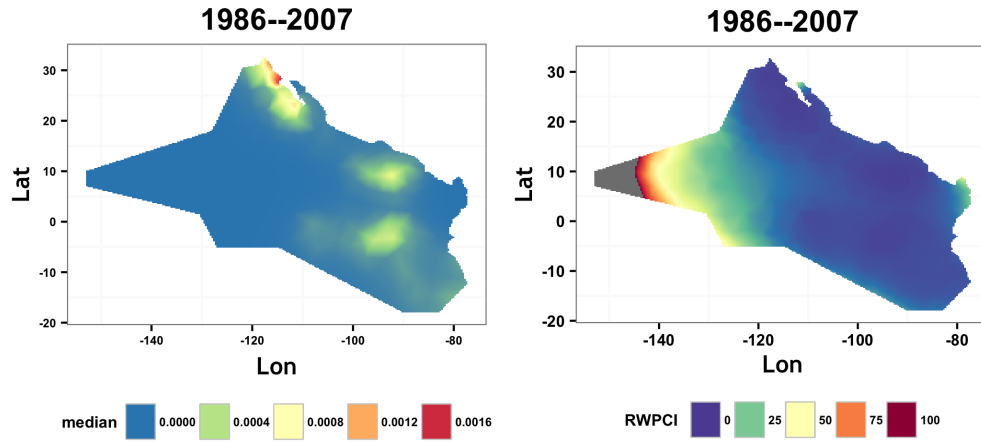


FIG 8. Posterior density of the blue whale groups using Model 0 in Table 1. The left panel displays the posterior median of the number of blue whale groups per square kilometre, and the right panel displays the relative width of the posterior credible interval given by (4.5). Model 0 does not incorporate any temporal information, therefore the posterior results displayed here are the same for all years.

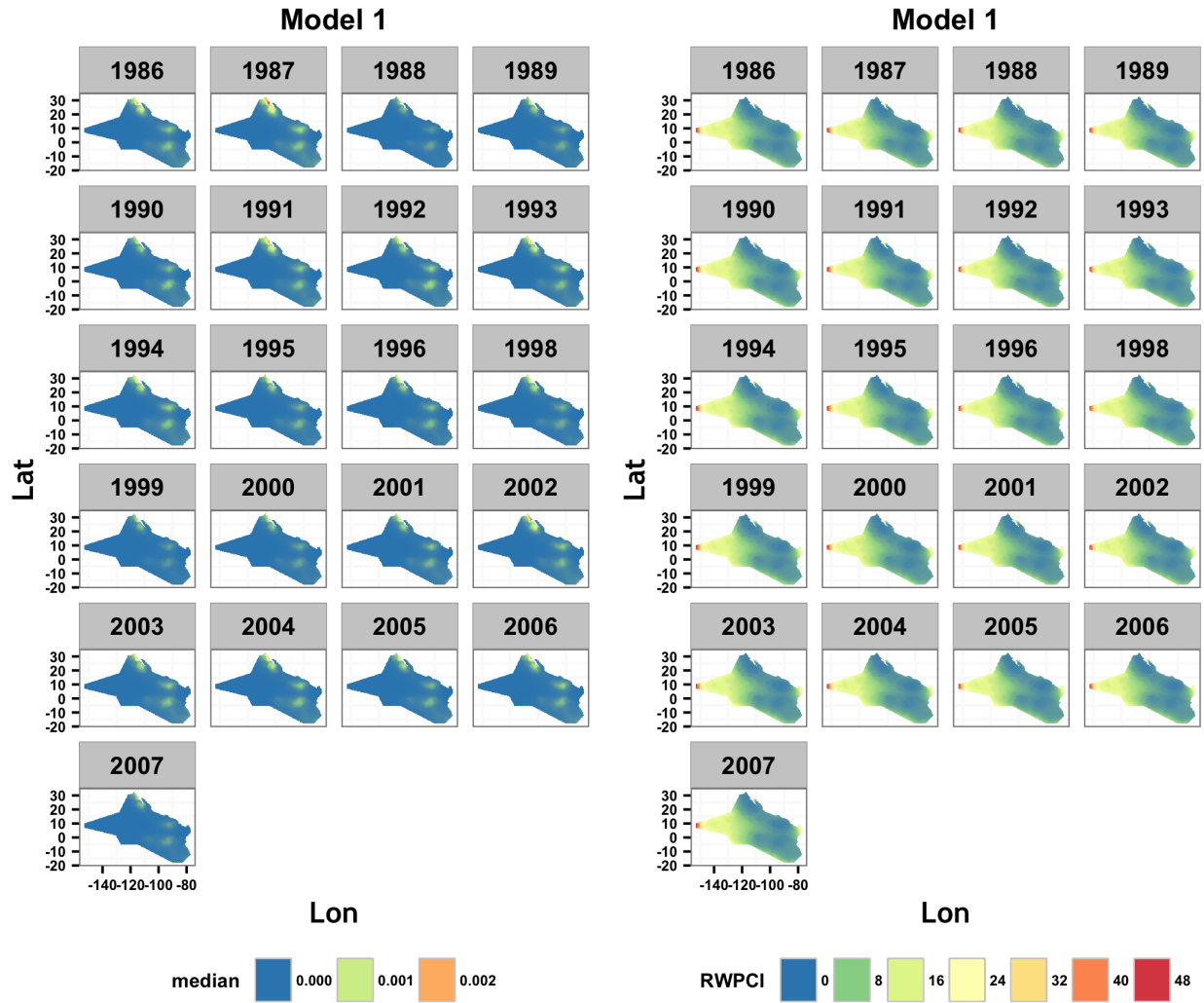


FIG 9. Posterior density of the blue whale groups using Model 1 in Table 1, years 1986–2007 (except 1997): the left panel displays the posterior median of the number of blue whale groups per square kilometre, and the right panel displays the relative width of the posterior credible interval given by (4.5).

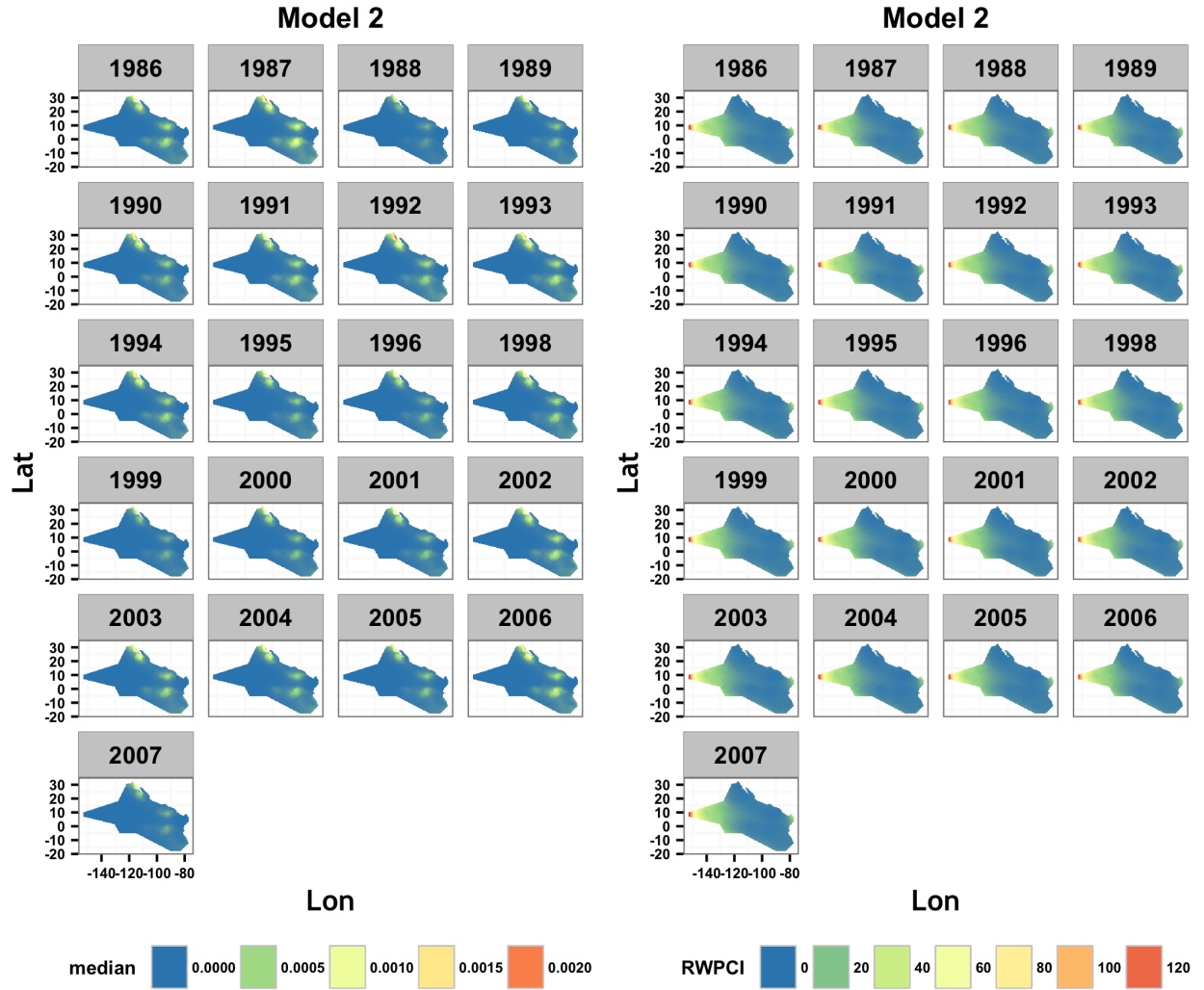


FIG 10. Posterior density of the blue whale groups using Model 2 in Table 1, years 1986–2007 (except 1997): the left panel displays the posterior median of the number of blue whale groups per square kilometre, and the right panel displays the relative width of the posterior credible interval given by (4.5).

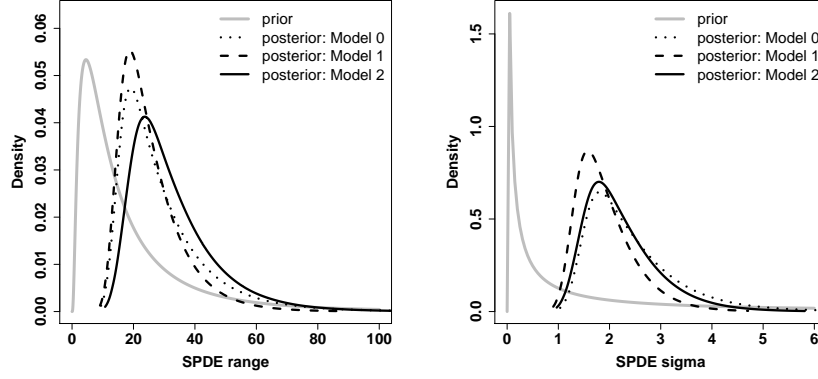


FIG 11. The posterior densities of the SPDE parameters using Models 0, 1 and 2 in Table 1. The left panel is for the range parameter ρ (see Section 2.5 for its definition), and the right panel for the marginal standard deviation σ_ξ in (B.1). In both panels, the dotted lines represent Model 0 and the dashed lines represent Model 1.1. The solid black lines represent Model 2.1 and the solid grey lines represent the priors for the SPDE parameters used in all three models (see Appendix E for the derivation of the SPDE priors).

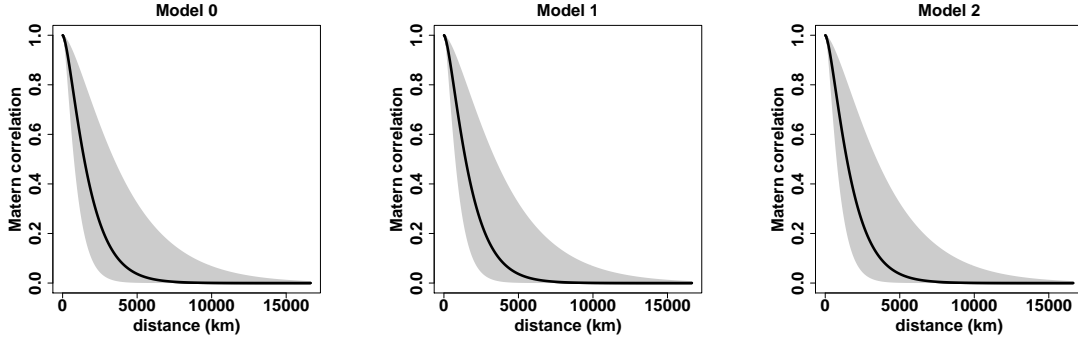


FIG 12. The Matérn covariance function (B.2) given the posterior estimates of κ for Models 0, 1 and 2 in Table 1. In all plots, the solid lines represent (B.2) with κ equal to its posterior median. The shaded area represents the range of (B.2) with κ values at its posterior 2.5% and 97.5% quantiles.

slowly varying standard deviation of the latent field in Fig 7 is likely due to a combination of large spatial range (see Fig 12 for the distance at which the spatial correlation drops to zero) and the fact that the observed point pattern is somewhat uninformative about the latent field.

SPDE parameters and detection function. We test different priors of the SPDE parameters for prior sensitivity. The posterior median of $\lambda(s; t)$ is less sensitive to different priors for the parameters than is the variance. Further details of the SPDE prior specification are given in Appendix E. Fig 11 displays the posterior densities of the SPDE parameters for Models 0, 1 and 2 using the same prior (the grey solid line). This figure shows small differences in the posterior densities among these three models, and an even smaller difference between Models 1 and 2 which use different centering schemes described in Section 4.2. Fig 12 plots the Matérn covariance as a function of Euclidean distance given the posterior estimates of the SPDE parameter κ in (B.2). Similar results are shown between different models. Model 0 has the widest credible interval, as expected, because this model does not use the information about the SST. The distance at which the spatial autocorrelation drops close to zero is quite large for three models, and this finding is consistent with the results of the latent Gaussian random field (ξ of (2.3)) shown in Fig 7. The posterior detection function with its 95% credible bands is shown in Fig 13, with little difference among Models 0, 1 and 2.

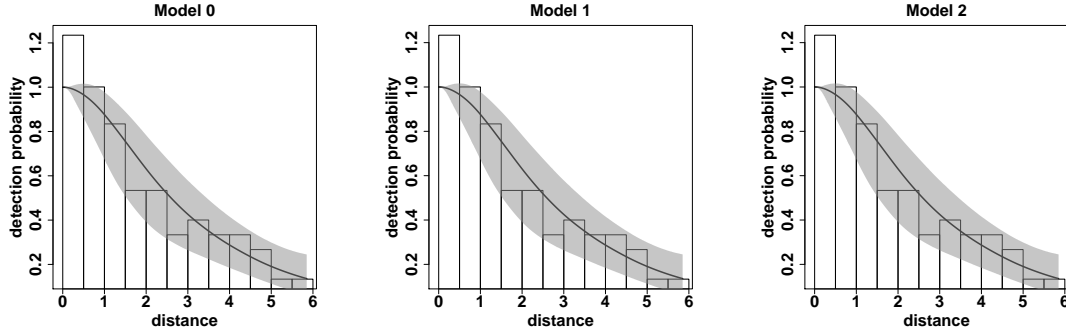


FIG 13. The posterior detection function with 95% credible band using Models 0, 1 and 2 in Table 1. The semi-parametric detection function is given in (2.6) and illustrated in Fig 2. The posterior credible band is calculated based on the posterior distribution of β 's in (2.6).

5. Discussion. This paper uses spatial point process methodology, in particular a flexible spatio-temporal log Gaussian Cox process, to model the spatial distribution of a population sampled using distance sampling methods. The most widely used methods for modeling spatial distribution from distance sampling surveys discretize space and aggregate the point pattern into counts with discrete spatial units (Buckland et al., 2015a; Miller et al., 2013). This results in a loss of the actual sighting locations and requires subjective decisions about the how to discretize space. Our spatio-temporal point process model preserves the sighting locations, models the effect of explanatory variables continuously in space, and unlike any existing method, also models spatial correlation that cannot be explained by such variables. It generalizes the approach of Johnson et al. (2010), which models density as a nonhomogeneous Poisson process, using actual sighting locations, but neglecting spatial correlation. Unlike Johnson et al. (2010), we do not assume spatial independence between observations, and use the SPDE/GMRF approach (Lindgren et al., 2011) to estimate the underlying spatial stochastic process and account for spatial dependence. Using INLA (Rue et al., 2009) for Bayesian inference, we build a hierarchical spatio-temporal point process model for the partially mapped point pattern observed by distance sampling (partially mapped because we only sample part of the survey area covered by transect lines for points).

It is rarely the case that spatial data are independent and assuming independence when data are dependent can lead to biased variance estimation, spurious significance of covariates, and overfitting (Cressie, 1993). Use of a GMRF allows us to model spatially autocorrelated random effects, and model patterns in residuals that cannot be explained by available covariates. As shown in Section 4.3, the spatial pattern captured by the GMRF in Fig 7 plays an important role in estimating the spatial distribution of ETP blue whale groups, shown in Fig 6. Because the underlying mechanisms that dictate the distribution of blue whales in space and time are probably quite complex, it is unlikely that SST alone could adequately explain the distribution, so that drawing inferences about the effect of SST based on a model without modeling spatial correlation may result in misleading biological interpretations.

For example, a previous analysis of these data by Pardo et al. (2015) modeled blue whale density spatially as a function of absolute dynamic topography (ADT), which, like SST, predicted fewer blue whales in warmer waters. However, because the model did not separate the temporal and spatial effects of ADT, large changes in ETP blue whale abundance were predicted from year to year, with few whales in warm (El Niño) years and many whales in cool (La Niña) years. Because blue whales have long life spans and reproduce slowly, and because tagging has shown that blue whales migrate to tropical waters every year, regardless of El Niño variations (see tracks in Bailey et al., 2009, for example), high interannual variation in true abundance seems unlikely. The hierarchical centering scheme in Section 4.2 separates the temporal and spatial effects of SST and accommodates situations in which whales make choices about habitat use

relative to the other choices available to them, and leads to a more biologically plausible model with less interannual variation. By also modeling spatial autocorrelation, our model does not run the risk of drawing biased inference about the effects of explanatory variables (SST here) due to unmodeled correlation.

The data structure we consider here differs from the point patterns typically analyzed in the point process literature (but see [Waagepetersen and Schweder, 2006](#)). These usually comprise a point pattern that has been observed in a finite observation window that is a subset of \mathbb{R}^2 , say. Unless finite point processes are explicitly considered the standard assumption then is that the point process continues in the same way outside the observation window. For interpretation, this implies that the analysis is only informative if the processes of interest are operating at a spatial scale that is captured within the (frequently single) subsample that is available. Further, there is an additional assumption that every point in the observation window has been observed, i.e. that the detection probability is one within the observation window and zero elsewhere.

When surveying wildlife, however, the processes of interest reflected in a spatial pattern, such as habitat preference, typically operate at a larger spatial scale than the sampled regions, and it is often impossible to fully sample an area that captures that scale. Here subsampling (transects in our case) is the norm and unlike in the situation discussed above, the spatial structures within the subsamples are not of primary interest, but the spatial behavior at a much larger scale is. Moreover a distinguishing feature of wildlife surveys is that detection probability is unknown and not one, even within the sampled region. This has often been dealt with in two stages, first estimating detection probability and then estimating spatial distribution conditional on the estimated detection probability. Our approach integrates the two, estimating detection probability simultaneously with the point process parameters.

We expect to see advances in spatio-temporal inference when there are covariates that affect both the thinning process and the density surface. Estimating the group size is difficult for animals that occur in groups such that not all animals in a group are visible simultaneously. The point process model in Section 2 can be extended to a marked point process model to incorporate group size in the model and allow detection probability to depend on group size. We also anticipate that our approach will be extended to deal with more complex observation processes and for other survey types – for spatial capture-recapture sampling ([Borchers and Efford, 2008](#); [Royle and Young, 2008](#)) for example, for situations in which detection probabilities change over time, or when there is unknown spatially varying sampling effort.

Acknowledgements. This research was funded by EPSRC grants EP/K041061/1 and EP/K041053/1. We thank the captains, crews and observers on the NOAA research vessels, and the support staff at the Southwest Fisheries Science Center, for the collection of line-transect data in the ETP over many years.

APPENDIX A: SOME ASSUMPTIONS

The assumptions referred to in Section 2.3 are as follows:

1. A team of observers is considered as a joint *black box* system, and the aggregated detection properties are modeled.
2. Individual objects (i.e. animals or animal groups) are not uniquely identified, only their locations are observed.
3. For each segment, the observable regions behind the starting point and ahead of the endpoint are small compared with the length of the segment as a whole, and the partial overlap of segments at changes in path direction is negligible.
4. The time between any other segment overlap is large enough that the time-slice point patterns in the overlap region can be considered independent; the object curves are considered to be in equilibrium, and at least locally mixing faster than the time between revisits by the observer.

APPENDIX B: SOME DETAILS OF SPDE MODELS

As noted in the body of the paper, the results from [Lindgren et al. \(2011\)](#) show how to take advantage of the connection between Gaussian Markov random fields of graphs and stochastic partial differential equations in continuous space. The most basic such model is based on the following stochastic partial differential equation (SPDE) defined on a 2-dimensional spatial domain

$$(B.1) \quad (\kappa^2 - \nabla \cdot \nabla)[\tau \zeta(\mathbf{s})] = \mathcal{W}(\mathbf{s}), \quad \mathbf{s} \in \mathbb{R}^2,$$

where $\nabla \cdot \nabla$ is the Laplacian, $\mathcal{W}(\mathbf{s})$ is Gaussian spatial white noise, and $\tau, \kappa > 0$ are variance and range scaling parameters. [Whittle \(1954, 1963\)](#) proved that stationary solutions to (B.1) are Gaussian random fields (GRF) with Matérn covariance function,

$$(B.2) \quad \text{cov} [\zeta(\mathbf{s}), \zeta(\mathbf{s}')] = \sigma_\zeta^2 \kappa \|\mathbf{s}' - \mathbf{s}\| K_1(\kappa \|\mathbf{s}' - \mathbf{s}\|), \quad \mathbf{s}, \mathbf{s}' \in \mathbb{R}^2,$$

where $\sigma_\zeta^2 = 1/(4\pi\kappa^2\tau^2)$ is the marginal variance, and K_1 is the modified Bessel function of the second kind and order 1. A measure of the spatial range can be obtained from $\rho = \sqrt{8}/\kappa$, which is the distance where the spatial correlation is approximately 0.13. More complex models can be obtained by changing the operator order or allowing the parameters to depend on the location. Spatio-temporal models can be constructed by either using a temporally continuous differential operator such as in the heat equation, or with auto-regressive constructions in discrete time, such as

$$(B.3) \quad \zeta(\mathbf{s}, t) = a \zeta(\mathbf{s}, t-1) + \omega(\mathbf{s}, t),$$

where $|a| < 1$ controls the temporal autocorrelation, and $\omega(\mathbf{s}, t)$ are solutions to (B.1), independent for each t . These constructions can also be directly applied to non-Euclidean domains such as the sphere, making construction of globally consistent random field models straightforward.

APPENDIX C: INTEGRATION SCHEME LINEARISATION

Consider a spatial integration scheme for a fixed time point. Reorganise the integration points from Section 3.2 so that \mathbf{u}_{kj} is integration point number j falling in triangle k , with $k = 1, \dots, K$ and $j = 1, \dots, J_k$. The corresponding integration weights are w_{kj} . For a given triangle we then obtain a linear approximation of function evaluations,

$$f(\mathbf{u}_{kj}) \approx \sum_{i=1,2,3} b_{kji} f_{ki},$$

where the b_{kji} are the Barycentric coordinates ([Farin, 2002](#)) of (\mathbf{u}_{kj}) with respect to the triangle and the f_{ki} denote the function f evaluated at the triangle vertices. It follows that the sum approximating the integration over a fixed triangle k can be carried out by three function evaluations,

$$\begin{aligned} \sum_{j=1}^{J_k} w_{kj} f(\mathbf{u}_{kj}) &\approx \sum_{j=1}^{J_k} w_{kj} \sum_{i=1,2,3} b_{kji} f_{ki} \\ &= \sum_{i=1,2,3} \left[\sum_{j=1}^{J_k} w_{kj} b_{kji} \right] f_{ki} \\ &= \sum_{i=1,2,3} \tilde{w}_{ki} f_{ki} \end{aligned}$$

with weights $\tilde{w}_{ki} = \sum_{j=1}^{J_k} w_{kj} b_{kji}$. Furthermore, vertices are shared among triangles. That is, f_a and f_b of two triangles a and b might refer to evaluations at the same mesh vertex. Hence, we can simplify the sum

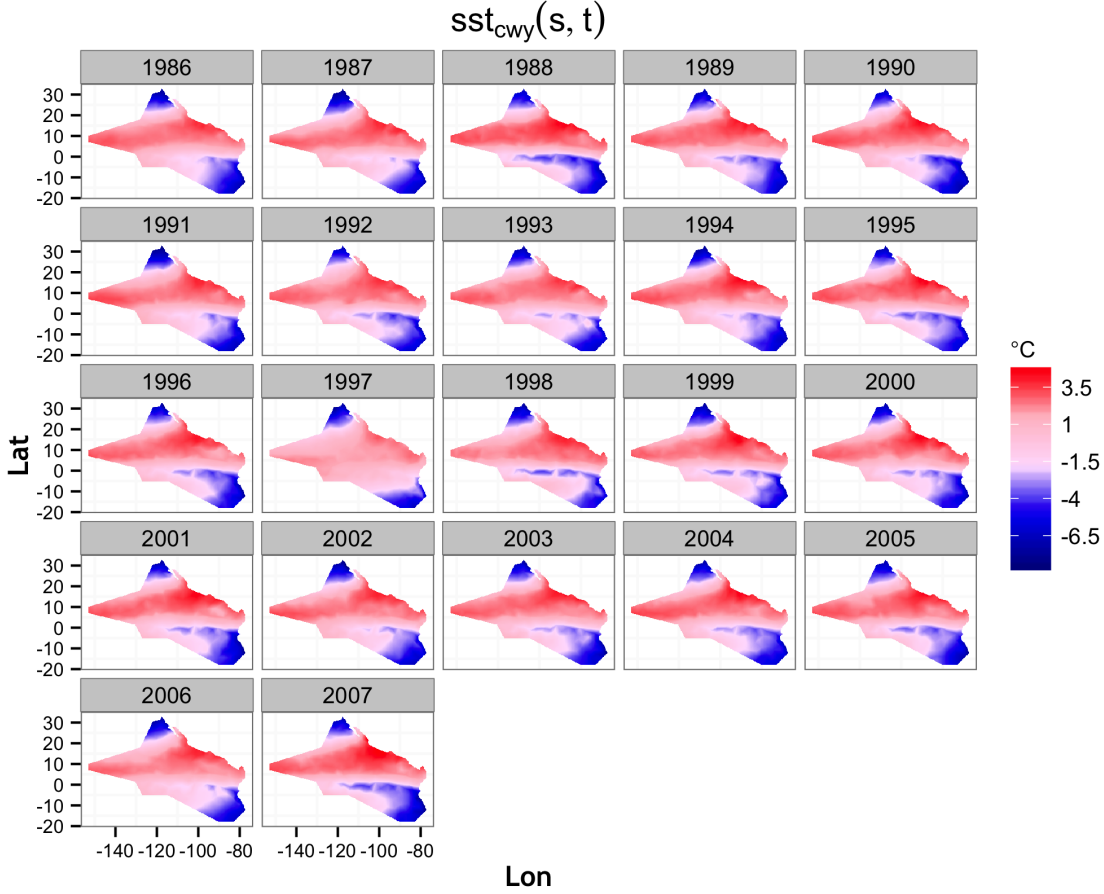


FIG 14. The SST centered within year for the ETP survey area when using the within-year centering scheme. $sst_{cwy}(s, t)$ is given by (4.2)

over all triangles as follows. Index the mesh vertices by $v = 1, \dots, V$ and let $v \sim (k, i)$ denote that v is the i -th vertex of triangle k . The (possibly empty) set of weights associated with vertex v then becomes $W_v = \{\tilde{w}_{ki}; v \sim (k, i)\}$ and we can write the full integral approximation as

$$\sum_{k=1}^K \sum_{j=1}^{J_k} w_{kj} f(\mathbf{u}_{kj}) \approx \sum_{v=1}^V \bar{w}_v f_v,$$

where f_v denotes a function evaluation at vertex v and $\bar{w}_v = \sum_{w \in W_v} w$.

APPENDIX D: MORE DETAILS ABOUT SST

In this appendix, we plot more details of the sea surface temperature (SST). SST is centered using the within-year and space-time centering schemes described in Section 4.2. The two components of SST when using the within-year centering scheme are the $\overline{sst}_c(t)$ in Fig 5 and $sst_{cwy}(s, t)$ in Fig 14, which have been defined in (4.1) by (4.2), respectively. For the space-time centering scheme, in addition to $\overline{sst}_c(t)$ in Fig 5, the remaining two components are displayed in Fig 15 and 16, where Fig 15 shows the spatial pattern of SST averaged over all years, and Fig 16 shows the residual SST. After subtracting the SST averaged over space (4.1) and SST averaged over time (4.3) from the SST displayed in Fig 4, the residual SST in Fig 16 shows residual patterns related to El Niño/La Niña oscillations, most clearly with the strong El Niño of 1997.

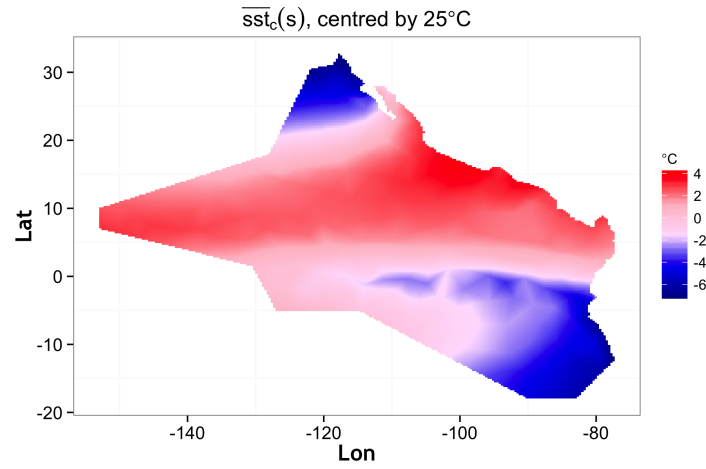


FIG 15. The time invariant spatial SST pattern $\overline{sst}_c(s)$ given by (4.3), where the overall average SST is $\overline{sst} = \int_{\Omega \times \mathbb{T}} sst(s, t) ds dt / (|\Omega| \times |\mathbb{T}|) \approx 25^\circ\text{C}$.

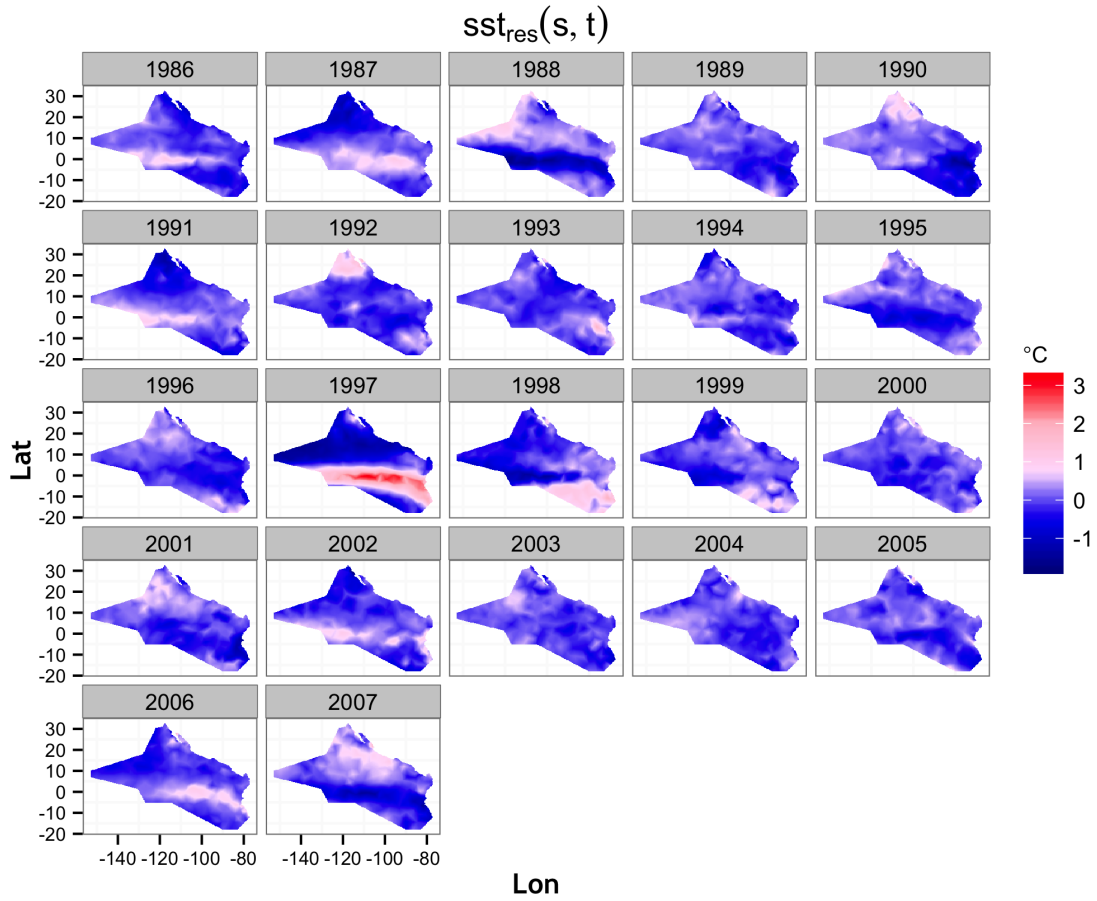


FIG 16. The SST residuals when using the space-time centering scheme. $sst_{res}(s, t)$ is given by (4.4).

APPENDIX E: SPDE PARAMETERS

R-INLA specifies the SPDE model using two internal parameters: κ and τ , both of which have an influence on the marginal variance of the random field σ^2 ,

$$\sigma^2 = \frac{\Gamma(\nu)}{\Gamma(\alpha)(4\pi)^{d/2}\kappa^{2\nu}\tau^2},$$

where ν is the smooth parameter and $\alpha = \nu - d/2$ with d being the dimension of the domain. In R-INLA, the default value is $\alpha = 2$. Whittle (1954) argues that it is more natural to use $\alpha = 2$ for $d = 2$ models than the fractional $\alpha = 3/2$, which generates exponential covariances. Rozanov (1982) shows that using integers for α gives continuous domain Markov fields, for which the discrete basis representation in Section 3.1 is the easy to construct. $\kappa > 0$ itself is related to the range parameter, denoted by ρ and $\rho = \sqrt{8\nu}/\kappa$. The range parameter ρ is commonly defined as the distance at which the spatial correlation function falls close to zero for all $\nu > 1/2$. Therefore, in our case of $d = 2$, we use $\alpha = 2$ and it follows that

$$(E.1) \quad \sigma^2 = \frac{1}{4\pi\kappa^2\tau^2} \quad \text{and} \quad \rho = \frac{\sqrt{8}}{\kappa}.$$

Working directly with the SPDE parameters κ and τ can be difficult, as they both affect the variance of the field. It is often more natural and interpretable to consider the standard deviation σ and spatial range ρ . The aim is to construct a joint prior for the internal model parameters κ and τ such that σ and ρ get independent log-Normal priors,

$$\begin{cases} \sigma \sim \text{logNormal}(\log \sigma_0, \sigma_\sigma^2), \\ \rho \sim \text{logNormal}(\log \rho_0, \sigma_\rho^2), \end{cases}$$

where σ_0 and ρ_0 are the prior medians.

First, we choose σ_0 and ρ_0 based on the problem domain. From (E.1), we obtain the corresponding values for the internal parameters κ and τ from $\kappa_0 = \sqrt{8}/\rho_0$ and $\tau_0 = 1/\sqrt{4\pi\kappa_0^2\sigma_0^2}$. Then, if τ and κ are parameterised through log-linear combinations of two parameters θ_1 and θ_2 ,

$$(E.2) \quad \begin{cases} \log(\tau) = \log(\tau_0) - \theta_1 + \theta_2, \\ \log(\kappa) = \log(\kappa_0) - \theta_2, \end{cases}$$

the σ and ρ parameters are related to θ_1 and θ_2 as

$$(E.3) \quad \begin{cases} \log(\sigma) = -\log(\sqrt{4\pi}\tau_0\kappa_0) + \theta_1, \\ \log(\rho) = \log(\sqrt{8}/\kappa_0) + \theta_2. \end{cases}$$

Thus, θ_1 and θ_2 separately control the standard deviation and spatial range, respectively. Assigning independent Normal distributions to θ_1 and θ_2 leads to the desired result, since $\log \sigma_0 = -\log(\sqrt{4\pi}\tau_0\kappa_0)$ and $\log \rho_0 = \log(\sqrt{8}/\kappa_0)$.

General guidance for how to choose the prior medians and variances is difficult to provide. Here, we use $\sigma_0 = 1$ and $\sigma_\sigma^2 = 10$ for the standard deviation, and $\rho_0 = \text{domainsize}/5$ and $\sigma_\rho^2 = 1$. The domain size for the ETP study is 62, and a fifth is a reasonable portion of that.

REFERENCES

- Bailey, H. B., Mate, B. R., Palacios, D. M., Irvine, L., Bograd, S. J., and Costa, D. P. (2009). Behavioural estimation of blue whale movements in the Northeast Pacific from state-space model analysis of satellite tracks. In *Endangered Species Research*, volume 10, pages 93–106.

- Borchers, D. L., Buckland, S. T., Goedhart, P. W., Clarke, E. D., and Hedley, S. L. (1998). Horvitz-Thompson estimators for double-platform line transect surveys. *Biometrics*, 54:1221–1237.
- Borchers, D. L. and Efford, M. G. (2008). Spatially explicit maximum likelihood methods for capture-recapture studies. *Biometrics*, 64:377–385.
- Brenner, S. C. and Scott, L. R. (2007). *The Mathematical Theory of Finite Element Methods*. Springer, New York, 3rd edition.
- Buckland, S. T., Anderson, D. R., Burnham, K. P., Laake, J. L., Borchers, D. L., and Thomas, L. (2001). *Introduction to Distance Sampling: Estimating Abundance of Biological Populations*. Oxford University Press, Oxford, UK, 1st edition.
- Buckland, S. T., Oedekoven, C. S., and Borchers, D. L. (2015a). Model-based distance sampling. *Journal of Agricultural, Biological, and Environmental Statistics*.
- Buckland, S. T., Oedekoven, C. S., and Borchers, D. L. (2016). Model-based distance sampling. *Journal of Agricultural, Biological and Environmental Statistics*, 21(1):58–75.
- Buckland, S. T., Rexstad, E. A., Marques, C. S., and Oedekoven, C. S. (2015b). *Distance sampling: methods and applications*. Springer.
- Cameletti, M., Lindgren, F., Simpson, D., and Rue, H. (2012). Spatio-temporal modeling of particulate matter concentration through the SPDE approach. *Advances in Statistical Analysis*, 97(2):109–131.
- Conn, P. B., Laake, J. L., and Johnson, D. S. (2012). A hierarchical modeling framework for multiple observer transect surveys. *PLoS ONE*, 7(8).
- Cressie, N., Calder, C. A., Clark, J. S., Ver Hoef, J. M., and Wikle, C. K. (2009). Accounting for uncertainty in ecological analysis: the strengths and limitations of hierarchical statistical modeling. *Ecological Applications*, 19:553–570.
- Cressie, N. A. C. (1993). *Statistics for Spatial Data*. New York: John Wiley & Sons.
- Diggle, P. J. (2003). *Statistical Analysis of Spatial Point Patterns*. Hodder Arnold, London, 2nd edition.
- Farin, G. E. (2002). *Curves and surfaces for CAGD: a practical guide*. Academic Press, 5th edition.
- Forney, K. A., Ferguson, M. C., Becker, E. A., Fiedler, P. C., Redfern, J. V., Barlow, J., Vilchis, I. L., and Ballance, L. T. (2012). Habitat-based spatial models of cetacean density in the eastern Pacific Ocean. *Endangered Species Research*, 16:113–133.
- Gerrodette, T. and Forcada, J. (2005). Non-recovery of two spotted and spinner dolphin populations in the eastern tropical Pacific Ocean. *Marine Ecology Progress Series*, 291:1–21.
- Gerrodette, T., Perryman, W., and Barlow, J. (2002). Calibrating group size estimates of dolphins in the Eastern Tropical Pacific Ocean. Administrative Report LJ-02-08. 20 p.
- Hayes, R. J. and Buckland, S. T. (1983). Radial-distance models for the line-transect method. *Biometrics*, 39(1):29–42.
- Hedley, S. L. and Buckland, S. T. (2004). Spatial models for line transect sampling. *Journal of Agricultural, Biological, and Environmental Statistics*, 9:181–199.
- Hedley, S. L., Buckland, S. T., and Borchers, D. L. (2004). Spatial distance sampling models. In Buckland, S. T., Anderson, D. R., Burnham, K. P., Laake, J. L., Borchers, D. L., and Thomas, L., editors, *Advanced Distance Sampling*, pages 48–70. Oxford University Press.
- Högmander, H. (1991). A random field approach to transect counts of wildlife populations. *Biometrical Journal*, 33:1013–1023.
- Högmander, H. (1995). *Methods of Spatial statistics in monitoring wildlife populations*. University of Jyväskylä, Jyväskylä.
- Illian, J. B., Penttinen, A., Stoyan, H., and Stoyan, D. (2008). *Statistical Analysis and Modelling of Spatial Point Patterns*. Wiley, Chichester.
- Illian, J. B., Sørbye, S. H., and Rue, H. (2012). A toolbox for fitting complex spatial point process models using integrated nested Laplace approximation (INLA). *The Annals of Applied Statistics*, 6:1499–1530.
- Johnson, D. S., Laake, J. L., and Ver Hoef, J. M. (2010). A model-based approach for making ecological inference from distance sampling data. *Biometrics*, 66:310–318.
- Johnson, D. S., Laake, J. L., and Ver Hoef, J. M. (2014). *DSpat: Spatial Modelling for Distance Sampling Data*. R package version 0.1.6.
- Kinzey, D., Olson, P., and Gerrodette, T. (2000). Marine Mammal data collection procedures on research ship line-transect surveys by the Southwest Fisheries Science Center. Technical report, National Oceanic and Atmospheric Administration, National Marine Fisheries Service, Southwest Fisheries Science Center.
- Kreft, I. G. G., de Leeuw, J., and Aiken, L. S. (1995). The effect of different forms of centering in hierarchicallinear models. *Multivariate Behavioural Research*, 30:1–21.
- Lindgren, F. and Rue, H. (2015). Bayesian spatial modelling with R-INLA. *Journal of Statistical Software*, 63(19).
- Lindgren, F., Rue, H., and Lindström, J. (2011). An explicit link between Gaussian fields and Gaussian Markov random fields: the SPDE approach (with discussion). *Journal of the Royal Statistical Society: Series B*, 73(4):423–498.
- Miller, D. L., Burt, M. L., Rexstad, E. A., and Thomas, L. (2013). Spatial models for distance sampling data: recent developments and future directions. *Methods in Ecology and Evolution*, 4:1001–1010.
- Miller, D. L., Rexstad, E. A., Burt, M. L., Bravington, M. V., and Hedley, S. L. (2014). *dsm: Density surface modelling of distance sampling data*. R package version 2.2.5.
- Møller, J., Syversveen, A. R., and Waagepetersen, R. P. (1998). Log Gaussian Cox processes. *Scandinavian Journal of Statistics*, 25:451–482.
- Møller, J. and Waagepetersen, R. P. (2004). *Statistical inference and simulation for spatial point processes*. Chapman & Hall/CRC,

- Boca Raton.
- Møller, J. and Waagepetersen, R. P. (2007). Modern statistics for spatial point processes (with discussion). *Scandinavian Journal of Statistics*, 34:643–711.
- Moore, J. E. and Barlow, J. (2011). Bayesian state-space model of fin whale abundance trends from a 1991–2008 time series of line-transect surveys in the California Current. *Journal of Applied Ecology*, 48:1195–1205.
- Niemi, A. and Fernández, C. (2010). Bayesian spatial point process modeling of line transect data. *Journal of Agricultural, Biological, and Environmental Statistics*, 15:327–345.
- Oedekoven, C. S., Buckland, S. T., Mackenzie, M. L., Evans, K. O., and Burger, L. W. (2013). Improving distance sampling: accounting for covariates and non-independency between sampled sites. *Journal of Applied Ecology*, 50:786–793.
- Oedekoven, C. S., Buckland, S. T., Mackenzie, M. L., King, R., Evans, K. O., and Burger, L. W. (2014). Bayesian methods for hierarchical distance sampling models. *Journal of Agricultural, Biological, and Environmental Statistics*, 19:219–239.
- Oedekoven, C. S., Laake, J. L., and Skaug, H. J. (2015). Distance sampling with a random scale detection function. *Environmental and Ecological Statistics*, 22:725–737.
- Pardo, M. A., Gerrodette, T., Beier, E., Gendron, D., Forney, K. A., Chivers, S. J., Barlow, J., and Palacios, D. M. (2015). Inferring cetacean population densities from the absolute dynamic topography of the ocean in a hierarchical Bayesian framework. *PLoS ONE*, 10(3):e0120727.
- Royle, J. A., Dawson, D. K., and Bates, S. (2004). Modeling abundance effects in distance sampling. *Ecology*, 85:1591–1597.
- Royle, J. A. and Dorazio, R. M. (2008). *Hierarchical Modelling and Inference in Ecology*. Academic Press, London, UK.
- Royle, J. A. and Young, K. V. (2008). A hierarchical model for spatial capture-recapture data. *Ecology*, 89:2281–2289.
- Roazanov, A. (1982). *Markov Random Fields*. Springer-Verlag, New York.
- Rue, H. and Held, L. (2005). *Gaussian Markov Random Field: Theory and Applications*, volume 104 of *Monographs on Statistics and Applied Probability*. Chapman & Hall, London.
- Rue, H., Martino, S., and Chopin, N. (2009). Approximate Bayesian inference for latent Gaussian models by using integrated nested Laplace approximations (with discussion). *Journal of the Royal Statistical Society: Series B*, 71(2):319–392.
- Schmidt, J. H., Rattenbury, K. L., Lawler, J. P., and Maccluskie, M. C. (2012). Using distance sampling and hierarchical models to improve estimates of dall’s sheep abundance. *The Journal of Wildlife Management*, 76(2):317–327.
- Simpson, D., Illian, J. B., Lindgren, F., Sørbye, S. H., and Rue, H. (2016). Going off grid: Computationally efficient inference for log-Gaussian Cox processes. *Biometrika*.
- Simpson, D., Lindgren, F., and Rue, H. (2012). Think continuous: Markovian Gaussian models in spatial statistics. *Spatial Statistics*, 1:16–29.
- Stoyan, D. (1982). A remark on the line transect method. *Biometrial Journal*, 24:191–195.
- Stoyan, D. and Grabarnik, P. (1991). Second-order characteristics for stochastic structures connected with Gibbs point processes. *Mathematische Nachrichten*, 151:95–100.
- van Lieshout, M. (2000.). *Markov point processes and their applications*. Imperial College Press, London.
- Waagepetersen, R. and Schweder, T. (2006). Likelihood-based inference for clustered line transect data. *Journal of Agricultural, Biological, and Environmental Statistics*, 11(3):264–279.
- Whittle, P. (1954). On stationary process in the plane. *Biometrika*, 41:434–449.
- Whittle, P. (1963). Stochastic processes in several dimensions. *Bulletin of the International Statistical Institute*, 40:974–994.
- Wiegand, T. and Moloney, K. A. (2014). *Handbook of Spatial Point-Pattern Analysis in Ecology*. Chapman & Hall/CRC.
- Williams, R., Hedley, S. L., Branch, T. A., Bravington, M. V., Zerbini, A. N., and Findlay, K. P. (2011). Chilean blue whales as a case study to illustrate methods to estimate abundance and evaluate conservation status of rare species. *Conservation Biology*, 25:526–535.
- Wolter, K. and Timlin, M. S. (2011). El Niño/Southern Oscillation behaviour since 1871 as diagnosed in an extended multivariate ENSO index (MEI.ext). *International Journal of Climatology*, 31:1074–1087.
- Wood, S. N. (2006). *Generalized Additive Models: An introduction with R*. Chapman & Hall/CRC, Boca Raton, FL, USA.

ADDRESS OF YUAN YUAN
SCHOOL OF MATHEMATICS AND STATISTICS
UNIVERSITY OF ST ANDREWS
THE OBSERVATORY, BUCHANAN GARDENS
ST ANDREWS, UK
KY16 9LZ
E-MAIL: yy84@st-andrews.ac.uk

ADDRESS OF FABIAN E. BACHL
SCHOOL OF MATHEMATICS
UNIVERSITY OF EDINBURGH
JAMES CLERK MAXWELL BUILDING
THE KING’S BUILDINGS
PETER GUTHRIE TAIT ROAD, EDINBURGH, UK
EH9 3FD
E-MAIL: fabian.bachl@ed.ac.uk

ADDRESS OF FINN LINDGREN:
SCHOOL OF MATHEMATICS
UNIVERSITY OF EDINBURGH
JAMES CLERK MAXWELL BUILDING
THE KING'S BUILDINGS
PETER GUTHRIE TAIT ROAD
EDINBURGH, UK
EH9 3FD
E-MAIL: finn.lindgren@ed.ac.uk

ADDRESS OF JANINE B. ILLIAN
SCHOOL OF MATHEMATICS AND STATISTICS
UNIVERSITY OF ST ANDREWS,
THE OBSERVATORY, BUCHANAN GARDENS
ST ANDREWS, UK
KY16 9LZ
E-MAIL: jbi@st-andrews.ac.uk

ADDRESS OF HÅVARD RUE
DEPARTMENT OF MATHEMATICAL SCIENCES
NORWEGIAN UNIVERSITY OF SCIENCE AND TECHNOLOGY
TRONDHEIM, NORWAY
N-7491
E-MAIL: Havard.Rue@math.ntnu.no

ADDRESS OF DAVID L. BORCHERS
SCHOOL OF MATHEMATICS AND STATISTICS
UNIVERSITY OF ST ANDREWS
THE OBSERVATORY, BUCHANAN GARDENS
ST ANDREWS, UK
KY16 9LZ
E-MAIL: dlb@st-andrews.ac.uk

ADDRESS OF STEPHEN T. BUCKLAND
SCHOOL OF MATHEMATICS AND STATISTICS
UNIVERSITY OF ST ANDREWS
THE OBSERVATORY, BUCHANAN GARDENS
ST ANDREWS, UK
KY16 9LZ
E-MAIL: steve@st-andrews.ac.uk

ADDRESS OF TIM GERRODETTE
NOAA NATIONAL MARINE FISHERIES SERVICE
SOUTHWEST FISHERIES SCIENCE CENTER
8901 LA JOLLA SHORES DRIVE
LA JOLLA, CALIFORNIA 92037, USA
E-MAIL: tim.gerrodette@noaa.gov